SCIENCE CHINA
Technological Sciences

•Article•

https://doi.org/10.1007/S11431-018-9478-4

Investigation on reversible pump turbine flow structures and associated pressure field characteristics under different guide vane openings

BINAMA Maxime[1], SU WenTao[2,1*], CAI WeiHua[1,3*], LI FengChen[4], WEI XianZhu[5], MUHIRWA Alex[1], GONG RuZhi[1] & WEKESA David W.[1]

[1]*School of Energy Science and Engineering, Harbin Institute of Technology, Harbin 150001, China;*
[2]*School of Energy and Power, Shenyang Institute of Engineering, Shenyang 110136, China;*
[3]*School of Energy and Power Engineering, Northeast Electric Power University, Jilin 132012, China;*
[4]*Sino-French Institute of Nuclear Engineering and Technology, Sun Yat-Sen University, Zhuhai 519082, China;*
[5]*State Key Laboratory of Hydropower Equipment, Harbin Institute of Large Electric Machinery, Harbin 150040, China*

Received September 10, 2018; accepted March 4, 2019; published online 0 ,

The use of reversible pump turbines (RPT) within pumped storage power plants goes with prolonged periods of off-design operating conditions, which leads to the onset of operating mode-dependent instabilities. In order to if not eliminate then decrease the gravity of RPT flow instabilities and associated damages, a deep understanding of its onset and development mechanism is needed. In line with this, the present study seeks to numerically investigate the onset and development mechanism of RPT unsteady flow structures as well as the evolutional characteristics of associated pressure pulsations throughout the RPT complete flow passage, under off-design conditions for three GVOs namely 17, 21, and 25 mm. The study results showed that low torque operating conditions and associated vaneless space back flow structures were the trigger of flow unsteadiness onset within the RPT vaneless space, the instabilities which grew to cause the s-shape characteristics appearance. Moreover, the runner flow unsteadiness was found to decrease with the GVO increase. On the other hand, the GVO increase worsened the pressure pulsation levels within RPT flow zones, where pressure pulsations within the vaneless space and flow zones in its vicinities were found to be the most sensitive to GVO changes.

reversible pump-turbine, flow unsteadiness, pressure pulsation, guide vane opening, numerical simulation

Citation: Binama M, Su W T, Cai W H, et al. Investigation on reversible pump turbine flow structures and associated pressure field characteristics under different guide vane openings. Sci China Tech Sci, 2019, 62, https://doi.org/10.1007/S11431-018-9478-4

1 Introduction

The exploitation of renewable energy sources (RES) has been a trend within the last decades [1,2], where hydropower and wind energy stand as the most massively exploited sources, with increasing generation numbers year after year. However, hydropower still outperforms all other RES where for instance in 2009, hydropower itself contributed 16% of the total global electricity generation and is projected to get to 75% in 2050 [3,4]. The advantages of hydroelectric power revealed itself almost as soon as national power grids started being fed by different types of power sources, where hydropower was praised for regulating the power network through its ability to compensate for abrupt load transients within the power grid (peak-looping), which later resulted into the birth of a specialized hydroelectric form known as pumped storage hydropower (PSP) [5,6]. Among the PSP

*Corresponding authors (email: suwentao305841@163.com; caiwh@hit.edu.cn, caiwh@hit.edu.cn)

advantages, a relatively high efficiency (65%–85%), large power capacity (typically 100–1000 MW), large storage capacity (1 to 24 h and plus), and a long life (30–60 years) at a low cycle cost ($0.1–$1.4/(kW h cycle)) [7,8] are the most remarkable, where their flexibility in terms of quick response to grid power randomness played a big role in their fast growing popularity. In a wind supplied power network for instance, the power grid may experience an unpredicted wind reduction leading to operating frequency deviation, thus creating a mismatch between power generation and grid load. Under these circumstances, PSP would quickly intervene and supply the make-up electricity to the grid in accordance with the grid load conditions at hand; and maintain the power grid nominal frequency for as long it takes the stability to get restored [9–11]. An example of such a case was given by Díaz-González et al. [12], where a PSP could inject from 0 to 1320 MW in the power grid in less than 15 s. PSPs use two reservoirs where during generation, the water is transferred from upper to lower reservoir, from where the same water is going to be pumped back to upper reservoir using the surplus energy during low consumption periods (night), thus accumulating more potential energy for later use [13–15]. In the early age, for the sake of achieving as high efficiency possible, PSPs used separate pumps and turbines for plant electromechanical equipment. However, with the PSP technological evolution, the application of Carnot theory led to a machine that can efficiently operate both as pump and a turbine, the one currently known as "reversible pump turbine" (RPT) [16]. Though PSPs have shown the ability to solve nominal frequency stability issues within the power grid, the control of RPT operations, where quick and frequent switch between generating and pumping modes with extended operations under off-design conditions is a routine, still poses quite a big threat to the plant operational safety [17]. In the past decades, energy generation actors used to run RPTs around their best efficiency point (BEP). But currently, for the sake of increased regulation capacity which in turn generates more revenues, RPTs are for most of times run under off-design operating conditions [18,19], thus serving a source to different flow stability-related problems [20–22]. Some of the already explored cases indicate that unstable operating conditions may be faced, under a constant guide vane opening (GVO), the machine operating characteristics curves (discharge-speed and Torque-speed curves) shift to an S-shaped configuration, an abnormality mostly referred to as "S shape characteristics" [23–25]. Under these conditions, one rotational speed may correspond to three discharges, which results in the occurrence of different detrimental phenomena such as the infliction of large pressure pulsations within the RPT flow areas, and the associated machine structural vibration and noise, all leading to an almost impossible machine synchronization with the power grid. In order to get a more detailed understanding about the cause behind RPT flow instability development, associated flow dynamics, as well as the influencing parameters be it design or operations-related, different studies have so far been carried out. Hasmatuchi et al. [26,27] and Wang et al. [28] investigated the RPT gradual flow instability development where severe pressure pulsations were noticed at runaway and got amplified in the turbine brake zone with stall cell development rotating at 70% of the runner speed and blocking some of runner flow channels. Botero et al. [29], through flow visualization and pressure sensing technics, investigated the RPT flow under turbine, runaway and turbine brake conditions. The flow characteristics moved from a stable state to runaway where flow separation and recirculation emerged, at the same time blocking some runner channels. Under turbine brake zone, the rotating stall was noticed, which consisted of four episodes, namely (1) a straight flow with rapidly increasing pressure; (2) flow stagnation; (3) highly disordered flow with decreasing pressure; and (4) sudden organization of flow. Li et al. [30], exploring the RPT transient flow characteristics, recorded serious pressure pulsations under speed-no-load conditions, taking source from a developed vaneless space water ring, which blocked the through-flow inducing pressure pulsations 3.8 to 8 times higher than the full load conditions. The same phenomenon was noticed by Wang et al. [31], where one stall cell was noticed at runaway, while four stall cells were recorded at lowest flow values. The blockage of runner flow channels by the developed stall was believed the main cause of sudden Head increase and the trigger of S-shape characteristics. This somehow agrees with Cavazzini et al. [32] findings where, in addition, it was stated that the onset of unsteady flow structures within the runner inter-blade channels is not enough to trigger the S-shape characteristics appearance. It was rather revealed that the S-shape characteristics develop only when the rotating stall is fully developed with a well-defined frequency. Widmer et al. [33] went deep on the description of RPT flow dynamics under both speed no load and low flow conditions for different GVOs. For small GVOs, when under low flow conditions, stationary and circumferentially distributed vortex flow emerged within the runner and vaneless space, blocking the guide vane flow, a phenomenon which led to increased pressure at upstream flow zones. The rotating stall cells on the other hand, were found to emerge within the runner and vaneless space, extending even to guide and stay vanes; when under large GVOs. These ones were found to successively block a number of channels, and rotated with subsynchronous speeds due to the moment exchange between the RPT stator and rotor compartments. The same RPT rotor-stator interactions and associated pressure pulsation characteristics were investigated by Zobeiri et al. [34] under maximum flow conditions, where the highest pressure pulsations amplitudes were recorded at the Blade passing fre-

quency (BPF) within the guide vane channels. The later quickly vanished within stay vanes whereas its double (2BPF) propagated until the spiral casing flow zones. Effect of cavitation on RPT pressure pulsations was studied by Liu and Guan [35], while Sun et al. [36] blamed the centrifugal forces and large flow incidence angle to be at the main cause of vortical flow structures development within the vaneless space which in turn led to S-characteristics appearance. Plant hydraulic transients and their influence on RPT S-shape characteristics were also investigated by Rezghi and Riasi [37], and Hu et al. [38].

Just as any other fluid machinery [39,40], the performance characteristics of RPTs depend very much on its components structural design. In line with this, attempting to tackle the RPT S-shape characteristics, Olimstad et al. [41] recommended different impeller modifications; increasing the blade length and the inlet blade angle among others. The blade meridional section broadening was recommended by Yin et al. [42]. The Influence of blade lean on RPT vaneless space pressure fluctuations was also studied by Zhu et al. [43]. On the other hand, Liu et al. [44] used multi objective optimization technic and improved the RPT runner efficiency. As for Pavesi et al. [45], the runner rotational speed can considerably influence the RPT pressure pulsation inception mode and their eventual development. Recently, Mao et al. [46] studied the flow field characteristics of an RPT with continuously closing guide vanes, where hydrodynamic conditions causing vibration under RPT load operating rejection conditions were explored. Both vortex flow development and the thickening of vaneless space water ring with the gradually decreasing flow; were blamed to be the triggers of increased pressure, head and torque fluctuations. The same feature was investigated by Li et al. [47] and Fu et al. [48,49], but now in the pumping mode.

Despite the fact that all these studies have provided important information about RPT flow instability, which so far led to some resolutional attempts; the causes and development mechanism of RPT flow instability are not yet fully understood, the reason why they are still thought as mythical phenomena. In their recently published article, Cavazzini et al. [50] stated that, in order to resolve the daily experienced power grid instability issues, the development of a new RPT concept is urgently needed. However, this must be founded on a deep and concrete understanding of RPT flow instabilities development mechanism. Generally speaking, a big number of carried out studies associated the occurrence of S-shape characteristics with different secondary flow structures development in RPT flow zones and resultant hydraulic losses, where the vaneless space between guide vanes and the runner has been the most reported flow instabilities base [51–53]. The guide vane ring is part of the flow control system within the RPTs and directly controls the angle with which the flow enters the runner, at the same time controlling the thickness of the stated vaneless space. It is then obvious that the change of GVO may lead to different hydraulic loss mechanisms, a process that need to be investigated in order to have an idea on the relationship between GVO angle and incurred flow patterns as well as the associated pressure pulsation variations. The present article's main intentions are therefore, to thoroughly investigate the RPT flow unsteadiness onset and development, and devise the influence of guide vanes opening on pressure pulsation characteristics within RPT flow zones. In this paper, 3D numerical simulations of the flow through a high-head RPT were carried out for four different operating conditions expanding from turbine operating conditions through runaway all the way down to the turbine brake zone; and that for three different GVOs, namely 17, 21 and 25 mm. The used RPT model was designed, built and tested at Harbin Institute of Large Electrical Machinery (HILEM) during the development of Jixi Hydropower plant in Heilongjiang Province, China. Performance characteristics for the RPT operations under the three GVOs were first presented to both validate the used numerical simulation scheme and showcase the presence of S-shape characteristics. Next, the flow field characteristics were analyzed to investigate the onset and eventual development of flow unsteadiness within RPT flow zones. Finally, an in-depth analysis of pressure pulsations both in time and frequency domain was carried out to mainly investigate their sources and the effect of GVO on their procession.

2 Research object and methods

2.1 Pump Turbine Model.

The experimentally investigated reversible pump turbine is a down-scaled model (1:7.533) of the real prototype installed at Jixi power plant in China. The experiments were carried out at Harbin Institute of Electric Machinery on a high-head hydraulic test rig. The pump turbine system model uses a single stage centrifugal type RPT of the specific speed N_s: 36.8 m^{-1}, with five main components namely; scroll casing, stay vanes, guide vanes, runner, and the draft tube. The external appearance of the used test rig and the tested pump turbine runner model are shown in Figure 1(a) and (b). Detailed geometrical characteristics of the RPT test section are also shown in Table 1.

In turbine mode, water was pumped from the underground reservoir to the inlet of the pump turbine's scroll casing, and then flowed through stay and guide vanes before whirling through the runner and exiting the test section through the draft tube back to the reservoir. Different measuring devices such as flowmeters and pressure sensors were used to get real time information on different flow characteristics at different flow zones within the pump turbine model. All the mea-

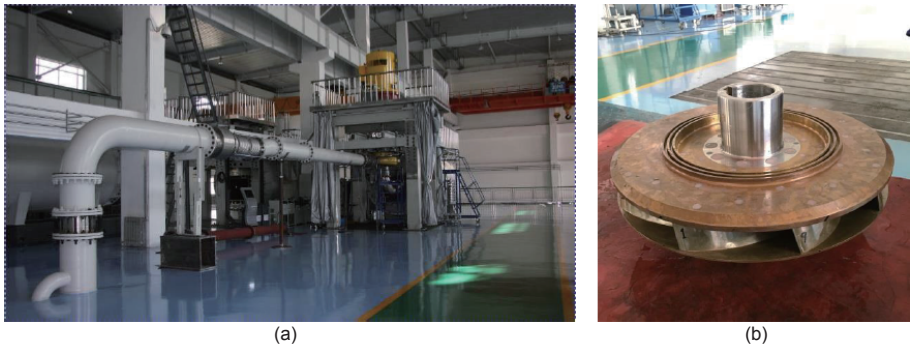

Figure 1 (Color online) Details about the HILEM Experimental test rig. (a) RPT hydraulic test section; (b) tested RPT model.

Table 1 Pump turbine model's geometric parameters

Parameter	units	Symbol	Value
Runner inlet diameter	mm	D_2	560
Runner outlet diameter	mm	D_1	270
Runner blade number	/	Z_R	9
GV distribution diameter	mm	D_V	662
Guide vane height	mm	B_V	37.8
Guide vane number	/	Z_V	20
Stay vane number	/	Z_S	20
Stay vane inlet diameter.	mm	D_{SI}	966
Stay vane outlet diameter.	mm	D_{SO}	763

surement were carried out in accordance to the International Electrotechnical Commission (IEC) standards [54], where tools like LabVIEW assisted by PXI-8336 controller were utilized to assure the highest accuracy possible.

The experimental tests on RPT external flow characteristics were successively carried out for 21 different GVOs ranging from 1 to 39 mm; where for each GVO, investigated operating points (Q_{11}-n_{11} and T_{11}-n_{11}) expanded from turbine, through runaway and turbine brake, all the way down to reverse pump quadrant as show in Figure 2. As it can be clearly seen from both figures, the S-shape characteristic is obvious at all the tested openings, where it is however found to be less pronounced for very small openings. The two vertical red lines display the nominal operating range. The unitary speed (n_{11}), flow (Q_{11}), and Torque (T_{11}) can be respectively defined as follows:

$$n_{11}=\frac{nD_1}{\sqrt{H}},\ Q_{11}=\frac{Q}{D_1^2\sqrt{H}},\ T_{11}=\frac{T}{D_1^3H}. \tag{1}$$

2.2 Numerical simulation scheme and validation

2.2.1 *Computational domain and grid details*

Experimental tests of turbulent flows through fluid machinery, even on a low scale level, can be very costly both in terms of financial resources and time. Moreover, some of hydrodynamic aspects of these flows may sometimes be very hard to capture. Numerical simulation under these conditions may serve a remedy to the stated shortcomings, thus leading to an adequate and quick fluid machinery performance characteristics prediction. In this study, 3D turbulent numerical simulations of the flow through a reversible pump turbine were carried out using a CFD commercial code Ansys CFX 18.0, under different operating conditions. The simulated RPT flow used the same route as in the experiments. The structural design of the reduced scale RPT model

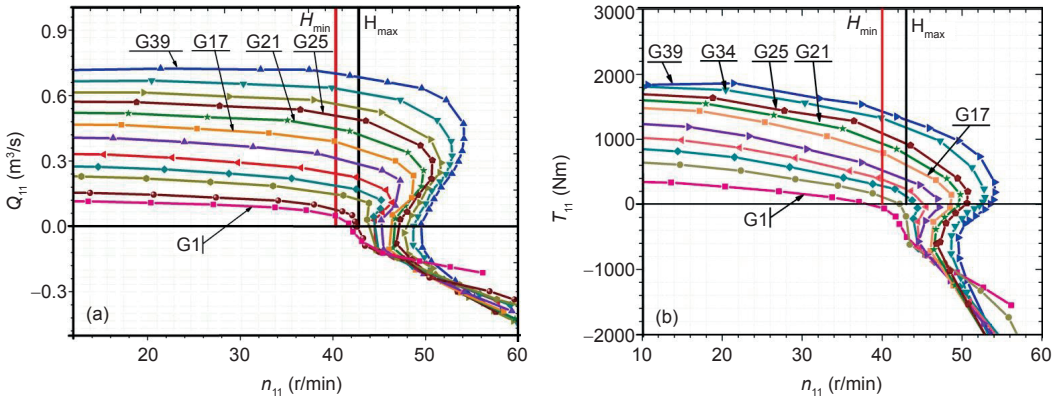

Figure 2 (Color online) The tested RPT's four quadrant characteristics with only two quadrants displayed. (a) Flow-speed (Q_{11}-n_{11}) curve; (b) torque-speed (T_{11}-n_{11}) curve.

and its system components, which is the investigated computational domain, was achieved using a computer aided design software, known as Unigraphics NX (Figure 3).

In order to predict the turbulent flow dynamics within the RPT, the grid for all RPT components has to be generated. The grid generation softwares Ansys ICEM and Turbo Grid were used to generate the structured hexahedral grid for most of components. The exception was made on the scroll casing tongue, where due to its sharp geometry, the unstructured tetrahedral grid mesh was adopted. Moreover, in order to ensure adequate flow details capturing within the boundary layer, finer mesh was created in the vicinities of solid walls at crucial flow zones such as runner blades, guide and stay vanes; where y^+ values globally ranged between 30 and 300. Note that y^+ is a commonly used measure of the distance of the first grid node from the wall. In the course of numerical simulation, the number of used grid nodes considerably influences the accuracy of simulated results. Therefore, six set of grid numbers ranging from 2.7 million to 11.4 million grid nodes were generated for the computational domain under consideration, and steady state numerical simulations were successively carried out on each of the sets under same inlet and outlet boundary conditions to verify the grid independence in terms of developed hydraulic head (Figure 4). It can be clearly seen that the RPT-developed head value varies for all grid numbers bellow 7.5 million, and almost stabilizes for grid numbers above. Therefore, in line with the available computational resources, a grid with 7.5 million grid nodes was chosen for the next transient simulations of turbulent reversible pump turbine flows in generating mode, under different operating conditions (Figure 5). The number of nodes for each component of the computational domain for the chosen computational grid set is shown through Table 2.

2.2.2 *Turbulence modeling and numerical scheme validation*

The flow through RPT, just as it is the case for any other incompressible flows, is governed by conservation laws of

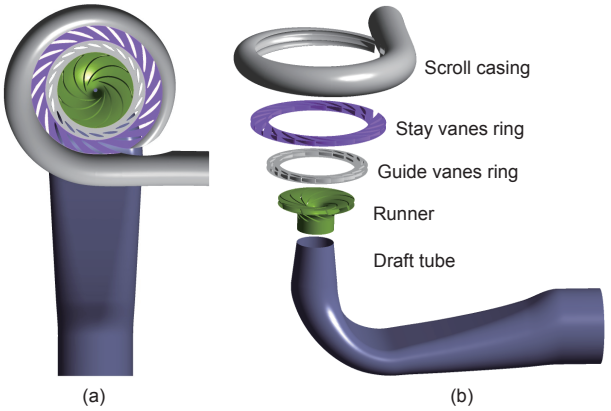

Figure 3 (Color online) Full RPT computational flow domain. (a) RPT model assembly; (b) RPT model components.

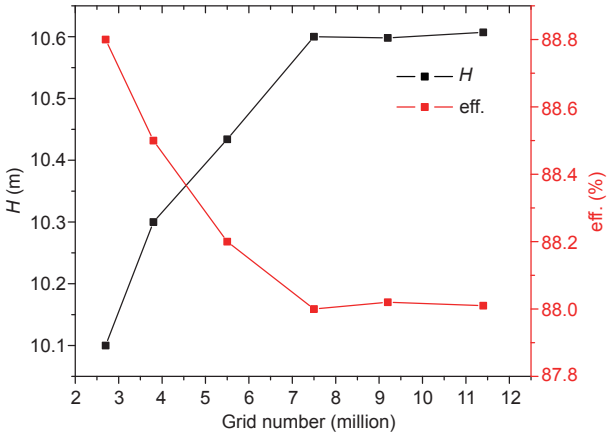

Figure 4 (Color online) Effect of grid number on RPT's hydraulic head and efficiency.

mass and momentum, commonly known as Reynolds Averaged Navier-stokes equations (RANS), and expressed in Cartesian coordinates as

$$\frac{\partial C'_i}{\partial x_i} = 0, \tag{2}$$

$$\frac{\partial \overline{C}_i}{\partial t} + \overline{C}_j \frac{\partial \overline{C}_i}{\partial x_j} = \frac{1}{\rho}\left(-\frac{\partial \overline{p}}{\partial x_i} + \mu \frac{\partial^2 \overline{C}_i}{\partial x_j^2}\right) - \frac{\partial \overline{C'_i C'_j}}{\partial x_j} + f_i. \tag{3}$$

Trying to close the above given conservation equations, turbulence models are required, where indeed different models have so far been developed and used in different cases, each with their advantages and weaknesses. Among the most used models for industrial problems, Jones and Launder [55] and Wilcox's [56] k-ε and k-ω models are on high statics, where the first expresses the turbulent eddy viscosity in terms of the turbulent kinetic energy k and its dissipation rate ε, whereas the second expresses it as a function of k and the turbulent frequency ω [57]. The k-ε model is known to perform better in the free streams far away from the wall but with remarkable inaccuracy for wall-bounded flows whereas k-ω is the opposite. Since the two models look complementary, Menter [58,59] introduced another model, the shear stress transport (SST), which combines them both, by finding the most appropriate turbulence model for each flow zones, using blending functions to get information about the distance to the closest wall [60]. Because of the RPT flow structures complexity especially under off-design conditions, the used turbulence model must have sufficient ability to accurately capture involved flow separations, both in the wall vicinities and the free flow zones [61]. So far, The SST turbulence model has been used for different RPT flow and pressure pulsation characteristics predictions, and the achieved accuracy has been quite satisfying [47,62–64]. Therefore, in this study, Menter's SST turbulence model is used to simulate the three-dimensional flow through the full passage of the investigated RPT model, where steady state simulations were first carried out, the

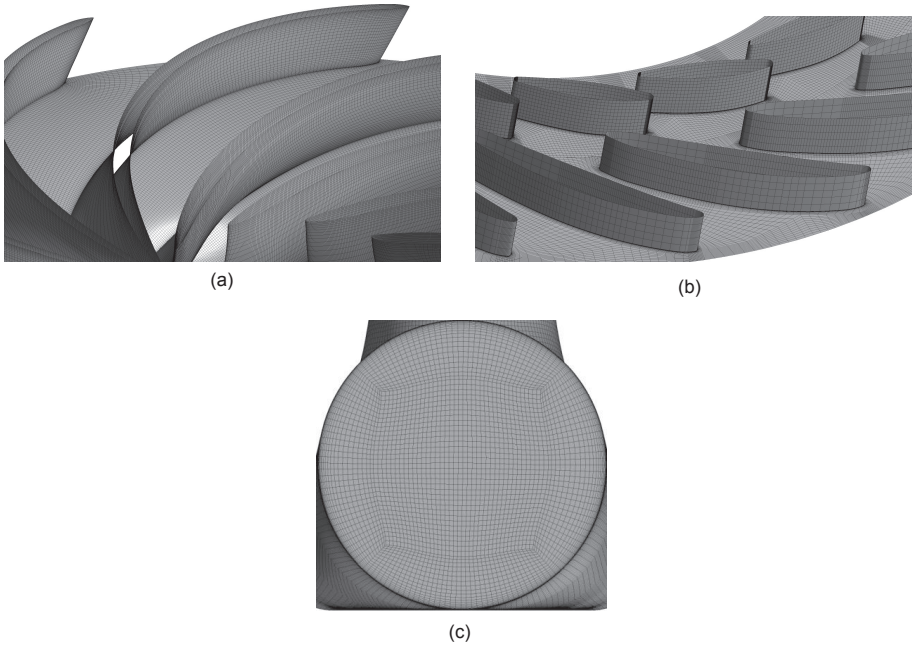

Figure 5 Used grid for different computational domain's components. (a) Impeller inter-blade channels; (b) guide and stay vanes flow zone; (c) draft tube outlet.

Table 2 RPT generated grid details

RPT components	Grid number ($\times 10^6$)	Grid type	Quality
Scroll casing	0.37	Hexahedral+unst.	0.3
Stay vane ring	0.53	Hexahedral	0.4
Guide vanes ring	1.05	Hexahedral	0.7
Runner	4.4	Hexahedral	0.35
Draft tube	1.15	Hexahedral	0.6
Total	7.5	–	–

results of which served as initial conditions of the followed transient simulations. In accordance with the experimental results, different discharge and static pressure values were correspondingly and successively imposed at the scroll casing inlet and draft tube outlet as inlet and outlet boundary conditions for different operating points (OP). The whole computational domain was divided into stationary (scroll casing, draft tube, stay and guide vanes) and rotating frames (runner), between which both the "stage mixing" and "frozen rotor-stator" interface types were applied for steady state simulations, while the "transient rotor-stator" interface type was used for transient simulations. The GGI interface type was used to match the scroll casing and stay vanes ring. The same interface type was used between the stay and guide vanes rings as well. The non-slip wall boundary conditions were imposed to all walls in the computational domain. The high resolution was chosen for both the advection scheme and turbulence numerics, while the second order backward Euler was used for transient scheme. A time-step equivalent to 1 degree impeller rotation was chosen, making one complete impeller revolution worth 360 time steps, where seven runner revolutions were simulated for each of the investigated operating points. The residuals Root-Mean-Square (RMS) was selected as the solution convergence criterion, where the convergence target was to set to be below 1×10^{-05} with 5 internal coefficient loops for each time step. Simulations were carried out on a medium capacity computer with Windows 7 Professional system installed. Processor: Intel(R) Core(TM) i7-5820KCPU@3.30GHz 3.30 GHz. Installed memory (RAM): 16.0 GB. System type: 64 bit operating system.

Transient numerical simulations were carried out for three different GVOs, namely 17, 21, and 25 mm; where for each GVO four different operating points (OPs) expanding from turbine (OP4) through runaway vicinities (OP6 and OP8) to turbine brake zone (OP9, OP10, and OP11), were selected and classified into four groups (GRO1 to GRO4) in accordance with their operating zones on the RPT flow-speed (Q_{11}-n_{11}) characteristics graph as shown in Table 3. The data used during computational simulations, such as inlet discharge (Q), runner rotational speed (n) and static pressure outlet (p), were taken from experimental test results. However, other performance characteristics such as the head (H), torque (T), and efficiency (η) were time-averaged values deducted from simulation results. Figure 6 shows that experimental and numerical results in terms of unitary values of speed (n_{11}), flow (Q_{11}), and torque (T_{11}) are in a quite acceptable agreement, with errors globally below 3% for points in the normal turbine operating zone. However, for points in the low discharge zones, the accuracy went a little bit weaker. The mismatch between numerical and experimental results may have taken source from the fact that different

Table 3 Investigated operating conditions and group classification

Operating groups	Operating points	n_{11} (r/min)	Q_{11} (m^3/s)	Operating zones
Group1 (GRO1)	G17-OP4	31.1032	0.427234	Turbine zone (high flow)
	G21-OP4	35.07734	0.48583	
	G25-OP4	36.474788	0.535297	
Group2 (GRO2)	G17-OP6	46.751665	0.300086	Turbine zone (low torque)
	G21-OP6	48.08953	0.33907	
	G25-OP6	49.441245	0.370482	
Group3 (GRO3)	G17-OP8	48.513019	0.130224	Runaway vicinities
	G21-OP8	49.52825	0.18238	
	G25-OP8	50.625762	0.218096	
Group4 (GRO4)	G17-OP9	46.429407	0.052416	Turbine brake (low flow)
	G21-OP10	46.73724	0.03509	
	G25-OP11	47.258613	0.032344	

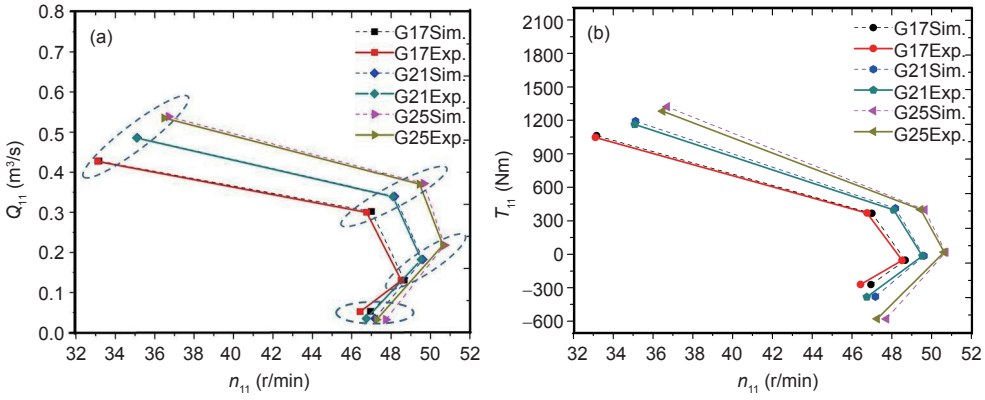

Figure 6 (Color online) Investigated operating points in the first quadrant for different guide vane openings. (a) Q_{11}-n_{11} graph; (b) T_{11}-n_{11} graph.

flow regions have been ignored such as the runner back and front chambers. Therefore, leakage losses and mechanical friction losses have not been included in numerical simulations which also contributed on the obtention of erroneous values in terms of available hydraulic head. However, the comparison of experimental and numerical simulation results on a global scale shows that the used numerical scheme could quite acceptably predict the RPT performance characteristics, thus confirming its trustworthiness.

3 Results and discussion

3.1 Flow field characteristics and evolution

In order to get more information on the onset and development mechanism of flow unsteadiness and the dynamics behind them within the RPT flow channels, RPT flow structures were first analyzed. As shown in Figure 7, the mid-span flow stream lines within the runner inter-blade flow zones are displayed, for the three investigated GVOs (17, 21, and 25 mm). Flow velocity decreases from turbine to turbine brake operating conditions in correspondence with the decreasing flow discharge, where higher flow velocity zones are located within the vaneless space for each of GVOs. Moreover, as the flow discharge decreased, flow streamlines got more and more disturbed leading to a complete blockage of some runner inter-blade flow channels at low flow conditions.

For operating conditions in GRO1, large flow vortices emerged at each blade's suction side. These runner blade suction side-attached vortical structures got weaker under GRO2 conditions, transferring a big portion to the runner blade inlet tips, which as a result, enhanced flow separations at the runner inlet and the adjacent Vaneless space. Under GRO3, vortical flow structures emerged within the inter-blade channels, but now with a gradually changing flow incidence angle at the runner inlet, these vortices shifted their locations from blade suction side to the pressure side. Note that these conditions represent the operating conditions right close to the runaway conditions. The runner blade pressure side-attached vortex got stronger, blocking some of the runner channels.

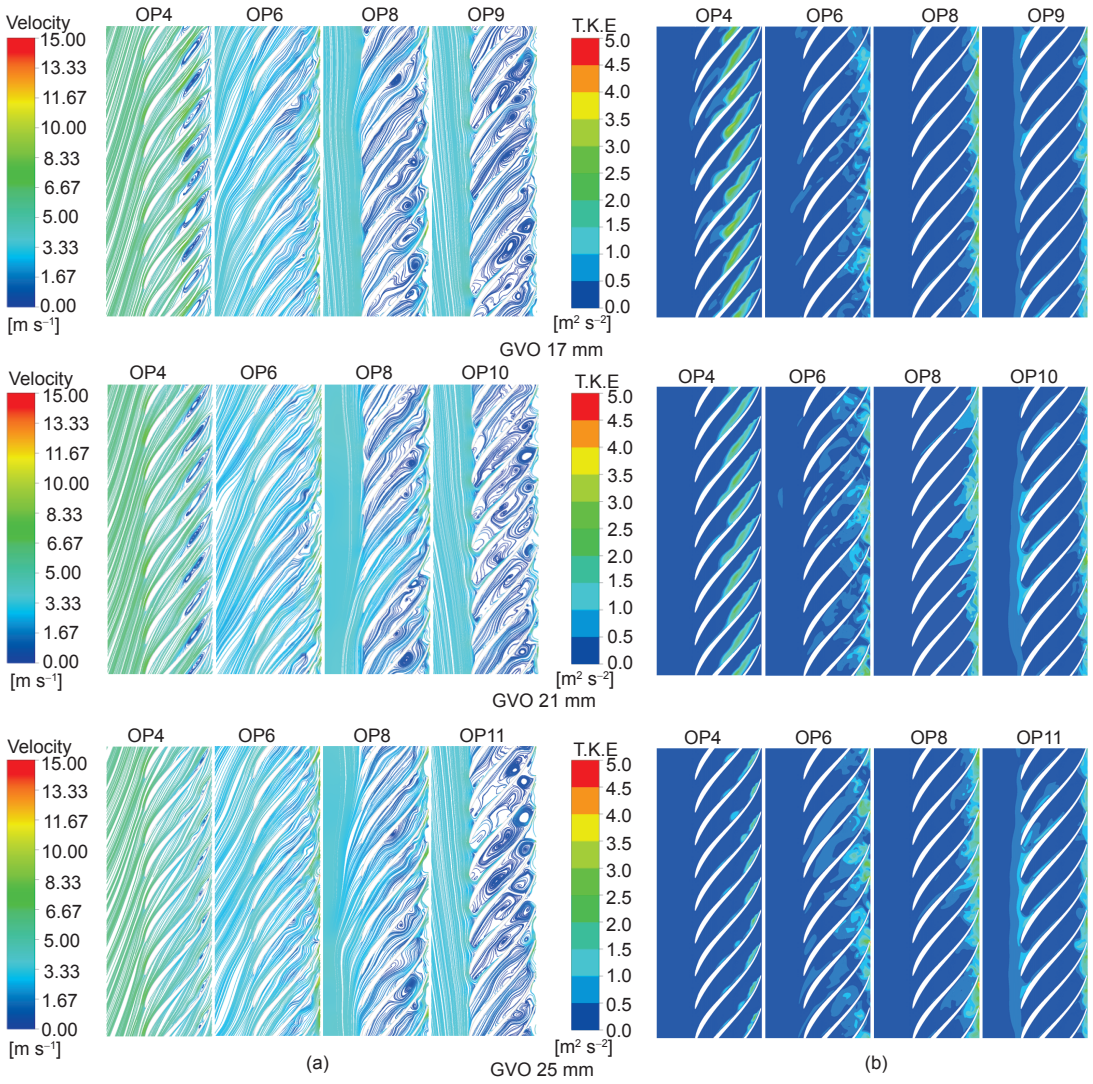

Figure 7 (Color online) Flow field characteristics within the runner inter-blade channels for the three guide vane openings at the mid-span section. (a) Velocity-colored flow streamlines at the runner midspan section; (b) turbulence kinetic energy contours at the runner midspan section.

Moreover, the vaneless space flow got more disturbed, where the flow instabilities merged even in the guide vanes forming an obvious flow circular ring between the stay and guide vanes [46]. The ring which got wider and stronger at low flow discharges close to zero discharge in the turbine brake zone (GRO4). Under low flow discharge conditions (GRO4), more runner inter-blade channels were blocked leading to more back flow to the vaneless space, thus increasing instability strengths in the same zones. Under these conditions, back flow vortical structures emerged even within upstream flow zones successively blocking a number of channels both in the guide and stay vanes. This phenomenon was believed to be the source of the RPT operating mode reversal behavior or experienced negative torques when under low flow discharge conditions. The hydraulic losses associated with the noticed flow unsteadiness are also believed to be at the source of S-shape characteristics emergence. Moreover, one can notice that the RPT vortex structures and their dynamics are obviously dependent on the GVO. However, the law guiding the relationship existing between the GVO and the RPT incurred flow structures was a bit complex.

As shown in Figure 7(a), the increase in GVO reduced the flow unsteadiness within the RPT flow zones for higher flow discharge conditions (GRO1–GRO3). The above mentioned vortex flow in the runner inter-blade channels and the vaneless space water ring got weaker with the GVO increase. Under higher flow discharge and small GVO conditions (G17-OP4), owing to the smallness of inter-guide vane channels, the flow speed increased resulting into smaller flow incidence angle at the runner blade inlet tips, thus creating flow separation at the same zones. This flow unsteadiness extended downstream to inter-blade flow channels, where blade suction side-attached vortices emerged. The same vortex flow was observed even on the other two remaining operating conditions of GRO1. These vortices,

however, narrowed and eventually lost its strength with the increase of GVO. This inter-blade vortex flow weakening with GVO increase was also recorded for conditions in GRO2 and GRO3 as well, where however, with a continuously decreasing discharge the Inter-Blade Vortical flow (IBVF) moved to the blade pressure side as mentioned above. This law, however, could not be verified for flow conditions in GRO4. Figure 7(b) presents the flow turbulent kinetic energy (TKE) at the runner mid-span section for flow conditions in the four investigated operating groups. Note that the flow turbulent kinetic energy is fundamentally the mean flow kinetic energy per unit mass associated with flow eddies, and is more connected to the physical RMS velocity fluctuations. In a complete agreement with GRO1 flow streams in Figure 7(a), high TKE zones for flow conditions were located at blade suction sides and gradually narrowed with the increase of GVO. On the other hand, for flow conditions in GRO2–GRO4, high flow TKE zones were located at runner inlet and vaneless space, and happened to widen up with the increase of GVO. Moreover, while GRO4 conditions are the most disturbed in Figure 7(a), they were still the ones with comparatively lower level of contained TKE in Figure 7(b).

This phenomenon may have taken source from the fluctuating flow velocity and its magnitude under low flow conditions, which is far lower as compared to high flow operating conditions case. Therefore, being basically related to the flow velocity, the TKE got lower with the exchanged momentum between runner and guide vane turbulent flows under low flow conditions. Figures 8 and 9 display the velocity-colored flow streamlines as well as the corresponding flow vorticity levels within the distributor flow zones, for the three investigated GVOs. The choice of vortex identification method is basically a quite complex process [65]. However, due to its suitability to vortex capturing within incompressible flows with tough vortical strengths, the Q-criterion method has been recommended and used by different investigators [49,66], making it the choice for this study (Figure 9). It can be seen that, in a quite similar way as Figure 7, the distributor inter-vane flow got messier as the flow decreased leading to back flow emergence within the stay and guide vanes at low flow conditions.

Moreover, the GVO happened to have a quite remarkable impact on the stated flow turbulence onset and development within the distributor flow zones, where flow unsteadiness was globally found to decrease with the increase of GVO, but that only for GRO1 to GRO3 operating conditions. The flow structures evolution for conditions under GRO4 were found to not follow any regular trend where GVO21mm-OP10 conditions were the most disturbed of the group. The same situation was quite similarly redisplayed through Figure 9. Basing on the fact that the vaneless space between runner and guide vanes has been labeled the base for RPT flow instability [67–69]; in order to have more information on the RPT flow unsteadiness onset and their development mechanism within this zone, flow structures at the same location and the adjacent runner inlet zones have been analyzed. Moreover, as the above discussed flow structures evolution aspects were only taken from one mid-span section, the presented truths may be of a partial importance. In order to have a wider view on the flow field characteristics and their eventual evolution, the analysis was carried out at span-wise cross-sections, expanding from hub to shroud sides. Figure 10 displays the runner inlet flow conditions for operating points expanding from high flow (GRO1) through turbine low torque conditions (GRO2) to low flow zone (GRO4) under 25 mm GVO. When under GVO25mm-OP4 conditions, the runner inlet flow streams enter the runner inter-blade channels very straight and smoothly with no induced back flow vortices (RFV). The flow velocity distribution was also almost uniform along the span wise direction. When the discharge decreased to GVO25mm-OP6, back flow vortices developed at the runner inlet's hub side, where flow velocity at the hub was far lower than that at the shroud. Under low discharge conditions (GVO25mm-OP11), BFV emerged even at the runner mid-span where the flow velocity was comparatively lower than the other two cases, but the velocity gradient between hub and shroud flows persisted. As shown through Figure 7(a) for all openings, the runner outlet flow streamlines under normal turbine operating conditions exhibit a trend where the flow velocity radial component has an obviously bigger influence on the flow domain than the tangential one (inclined streamlines at runner outlet). However, as the flow decreases at the same time the runner angular speed increasing, the tangential component takes over where it gets to its maximum under very low discharge conditions (obvious horizontal streamlines at the runner outlet). The same phenomenon exists at the runner inlet. With both the progressively decreasing discharge and increasing runner rotational speed, the flow velocity's radial component at the runner inlet correspondently decreases while the tangential one increases with the increasing runner rotation speed. When the velocity radial component gets to negative values, BFV appears at the runner inlet zones, most probably at the hub side. With farther decrease and increase of flow and runner angular speed respectively, the BFV get to their highest levels where they may transfer their operating locus to runner mid-span zones. Figures 11–13 show the velocity-colored flow streams along the streamline direction at three converging planes, expanding from runner through vaneless space to the guide vane ring, for three GVOs. Generally speaking, for all the operating conditions within GRO1, vaneless space flow is stable with almost no incurred vortices.

Under GRO2, vaneless space vortical structures emerged and obstructed the Hub flow, which later on caused the

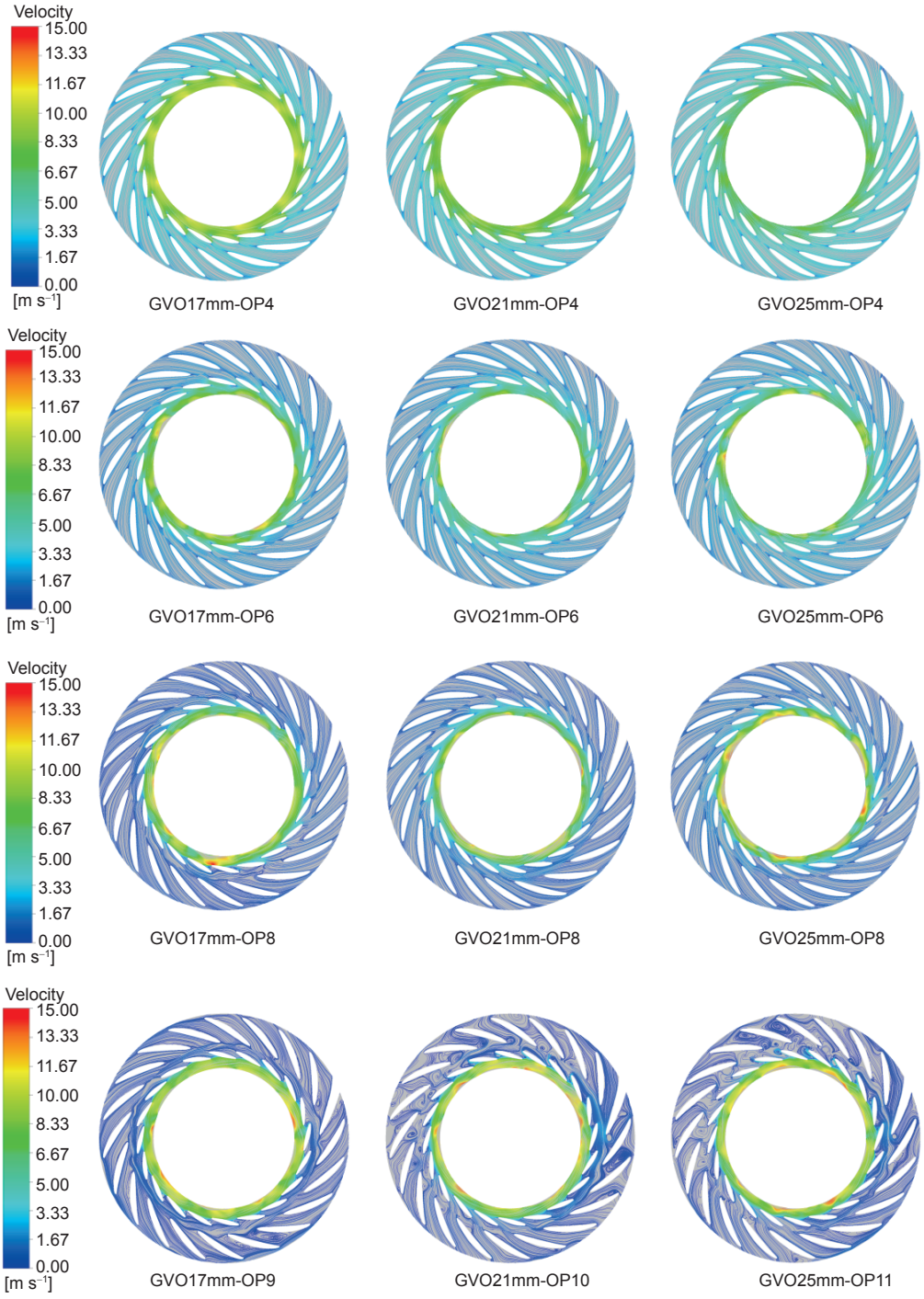

Figure 8 (Color online) Flow velocity-colored streamlines within guide and stay vane channels for three openings under four different operating conditions.

downstream stall evolvement within the inter-blade channels at the shroud. Under GRO3, the situation was different for different openings. GVO17mm-OP8 conditions were marked by the shift of vaneless space vortices from hub to mid-span zones, which remained the case even for corresponding low flow conditions (GVO17mm-OP9). However, for openings 21 and 25 mm, vortex flow remained at the hub where it finally shifted to mid-span region only when under lower flow conditions (GRO21mm-OP10 and GRO25mm-OP11). Therefore, it was found that the bigger the GVO, the longer it takes to get into S-shape region. Moreover, the location of vaneless space vortices somehow determines the position of inter-blade flow stall. When the vaneless vortices were at the hub, the downstream inter-blade stall formed in the runner shroud vicinities, when the vaneless vortex flow shifted to mid-plan region the inter-blade stall also formed in

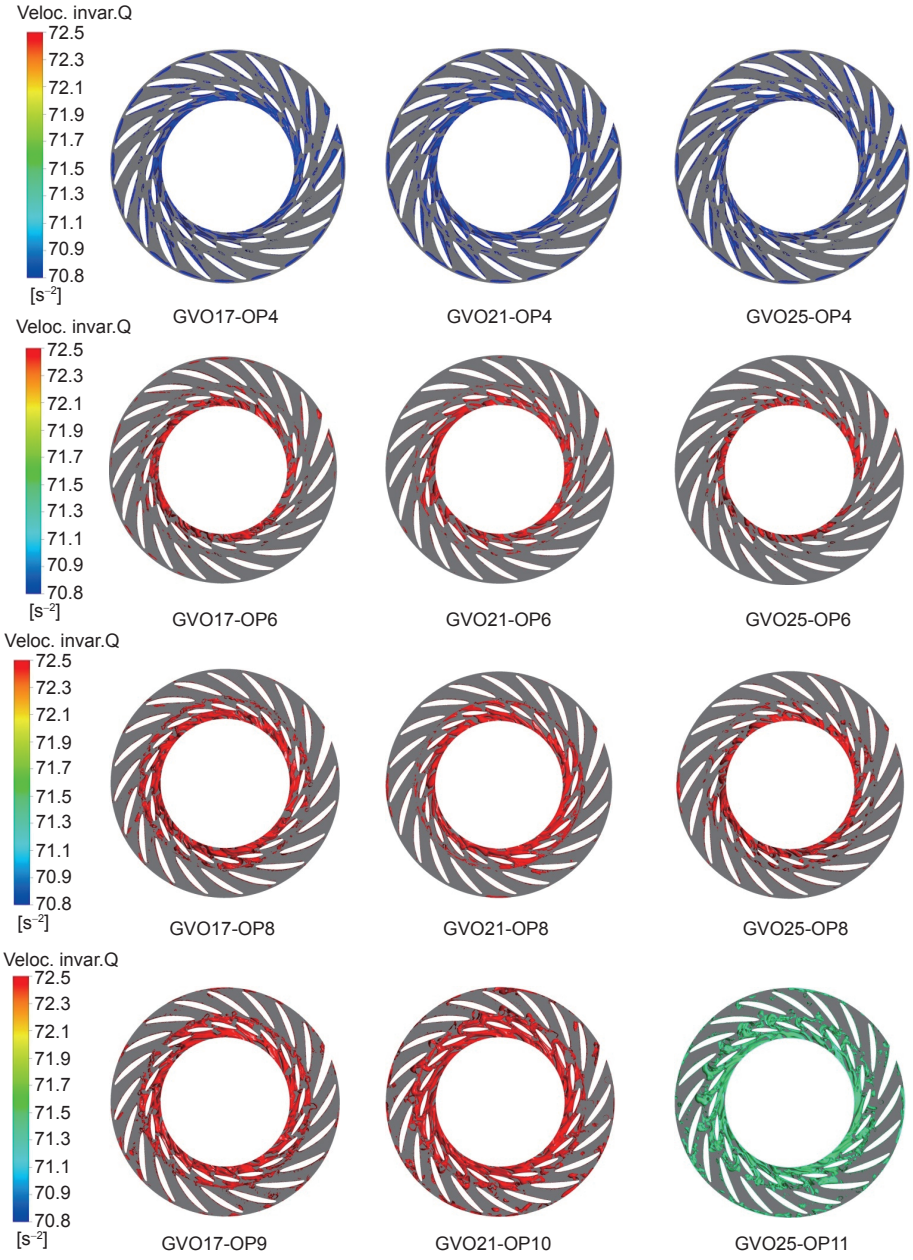

Figure 9 (Color online) Flow vortex distribution within guide and stay vane channels for three openings under four different operating conditions.

the run mid-pan region.

3.2 Pressure pulsation analysis

For a deeper analysis of pressure pulsation mechanism and its propagation modes, as well as their relationship with incurred flow structures within different RPT components, several pressure monitoring points were positioned at different locations within the RPT flow zones. Figure 14 shows such an arrangement within the spiral casing (Figure 14(a)), distributor (Figure 14(b)), and draft tube (Figure 14(c)). 36 pressure monitors (GU1–GU36) were circumferentially distributed within the vaneless space around the runner inlet zone, with a constant angular interval of 10°. Many more pressure monitors were positioned along the flow channels following the flow passage from the spiral casing (CP1A to CP4), through the RPT distributor, englobing both the interspaces of stay and guide vanes (ST10 to ST2 and GR4 to GR1 respectively), all along down to draft tube (DR1 to DR13). The eventual RPT flow structures evolution has been found to closely relate to pressure pulsation characteristics at hand. In order to clarify this relationship in a comparative way, pressure pulsation levels were quantified through a parameter referred to as the relative pressure pulsation amplitude (RPPA), which is expressed through the following equation:

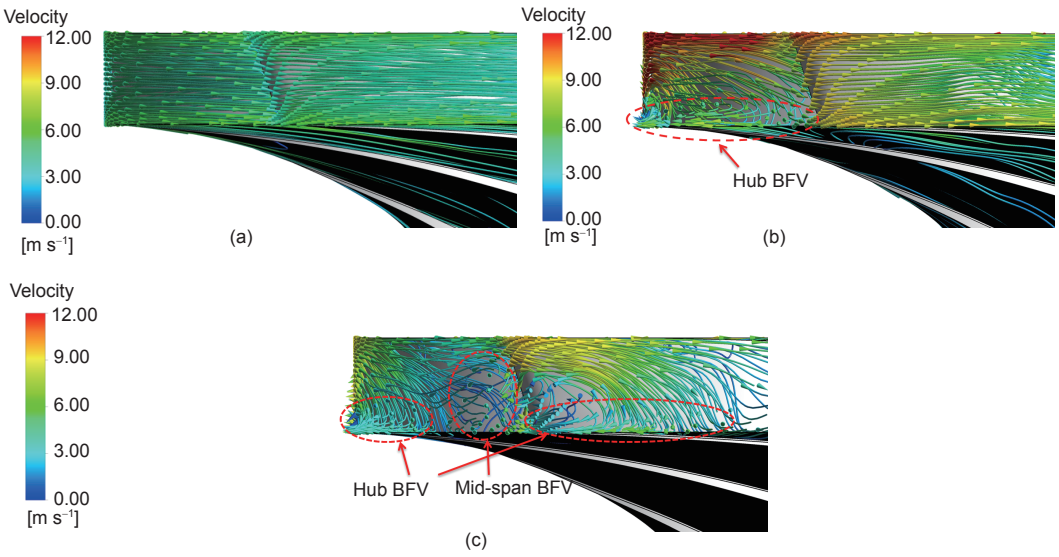

Figure 10 (Color online) Back flow vortices (BFV) at the runner inlet for different operating conditions under GVO 25 mm. (a) GVO25mm-OP4; (b) GVO25mm-OP6; (c) GVO25mm-OP11.

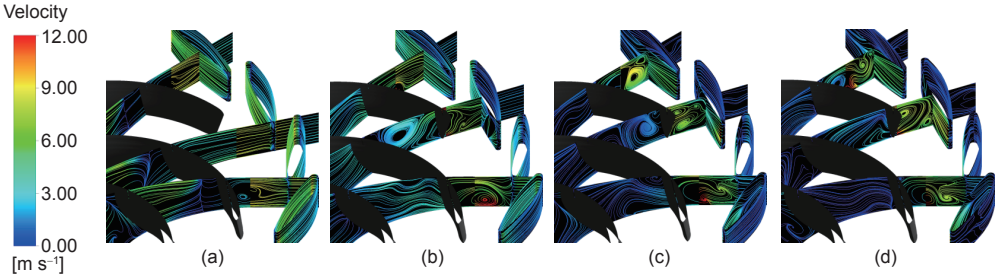

Figure 11 (Color online) Flow vortical structures at the inter-blade flow channels, runner inlet and vaneless space flow zones; for the GVO of 17 mm. (a) GVO17mm-OP4; (b) GVO17mm-OP6; (c) GVO17mm-OP8; (d) GVO17mm-OP9.

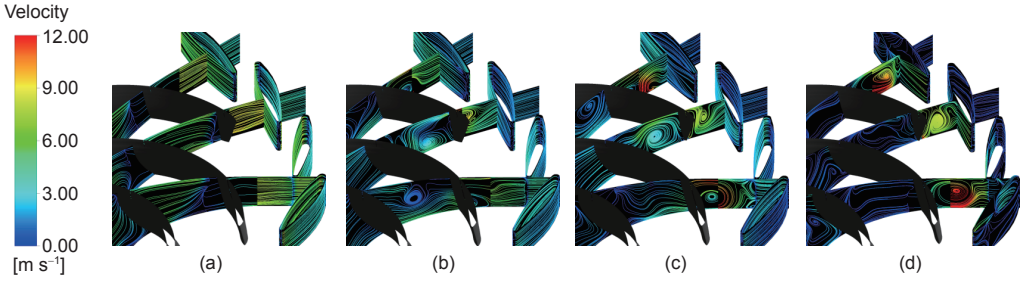

Figure 12 (Color online) Flow vortical structures at the inter-blade flow channels, runner inlet and vaneless space flow zones; for the GVO of 21 mm. (a) GVO21mm-OP4; (b) GVO21mm-OP6; (c) GVO21mm-OP8; (d) GVO21mm-OP10.

$$R_{\mathrm{A}} = \frac{(P_{\mathrm{imax}} - P_{\mathrm{imin}})}{\rho g H} \times 100, \tag{4}$$

where R_{A} is RPPA, $P_{\mathrm{i\,max}}$ and $P_{\mathrm{i\,min}}$ are individual maximum and minimum pressure pulsation amplitudes (PPAs) respectively, ρ is the water density, g is gravitational acceleration and H is the hydraulic head. Three operating conditions were selected, namely high flow (GRO1), low torque (GRO2) and low flow conditions (GRO4). Figure 15 shows the vaneless space RPPAs distribution under three selected operating conditions for the three investigated GVOs. Under high flow conditions, the vaneless space pressure fluctuation amplitudes varied periodically around the runner inlet zone, and their distribution symmetry to the runner rotational axis position could be easily noticed. When back flow structures emerged at the runner inlet zone's hub side under low torque conditions, pulsation amplitudes substantially increased, reaching their highest values at flow zones next to the special vane (GU31-GU35); meaning that

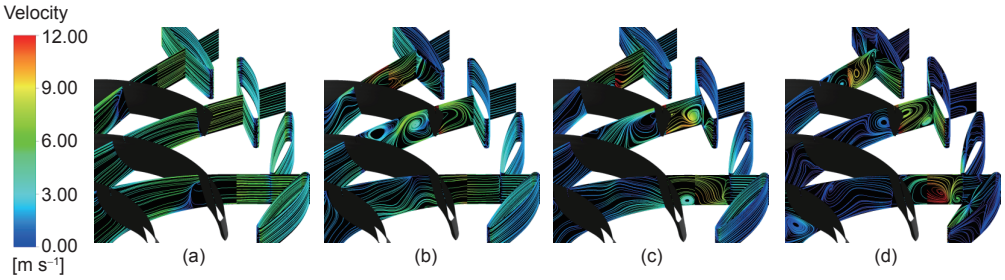

Figure 13 (Color online) Flow vortical structures at the inter-blade flow channels, runner inlet and vaneless space flow zones; for the GVO of 25 mm. (a) GVO25mm-OP4; (b) GVO25mm-OP6; (c) GVO25mm-OP8; (d) GVO25mm-OP11.

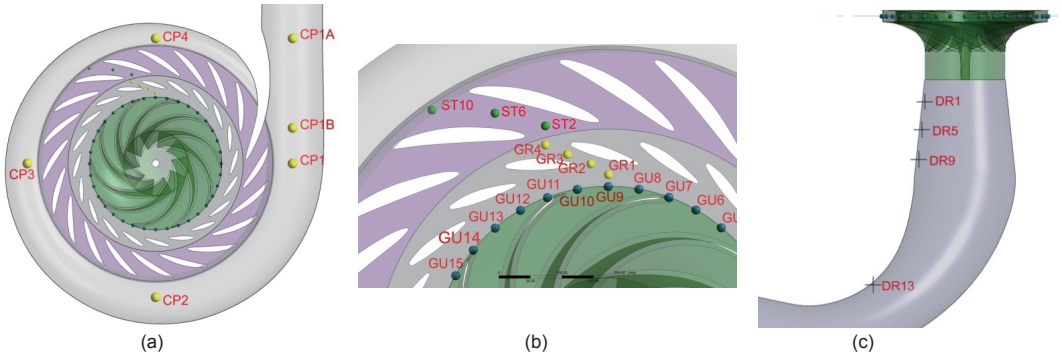

Figure 14 (Color online) Monitoring points locations. (a) Positions within the spiral casing; (b) positions within the inter-vane channels and runner inlet zones; (c) positions within the draft tube.

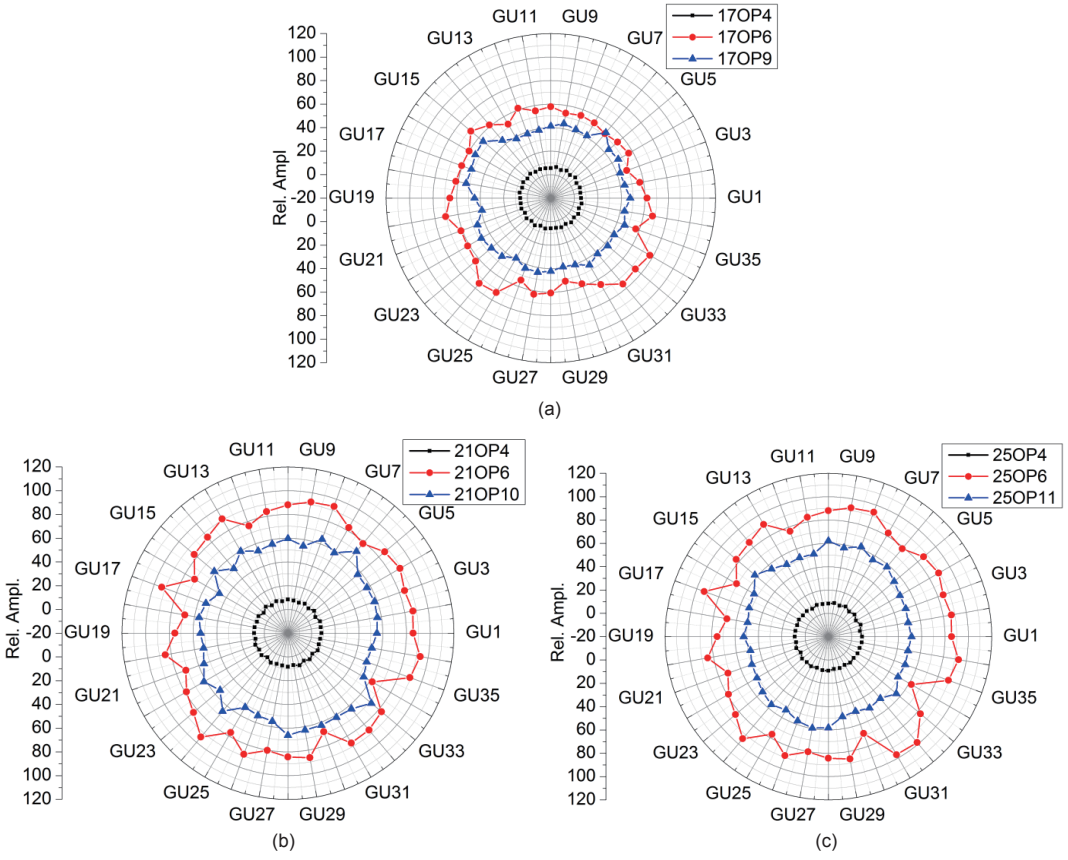

Figure 15 (Color online) Vaneless space relative pressure pulsation amplitude distribution for (a) GVO17mm, (b) GVO21mm and (c) GVO25mm.

the position of the special vane also has an impact on RPT pressure field characteristics.

Under these conditions, the similarity in terms of amplitude distribution trend for all the openings is quite obvious, but more pronounced for 21 and 25 mm openings. However, the symmetry and periodicity of the pressure fluctuation amplitudes distribution have not been noticed for this case. This may have taken source from the emergence of different flow unsteadiness in the vaneless space, where random inter-blade flow channel blocking by the uprising vortex flow at the same zones, took place. Under low flow conditions however, the randomness in terms of PPA distribution persisted with a bit of improvement, but PPAs decreased to lower values than the low torque case. Figure 16 displays the frequency spectra at different positions within the vaneless space for the three investigated operating conditions (OP4, OP6, and OP10) under 21 mm guide vane opening. For all the three conditions, the BPF and its harmonics are the dominant frequencies, where BPF is the first dominant frequency, 2BPF the second, and 3BPF the third.

In total agreement with Figure 12(a), the high flow operating conditions are characterized by a stable and smooth flow at the runner inlet with no back flow vortices available, therefore pressure pulsations within the vaneless space are only due to rotor-stator interactions (RSI, see Figure 16(a)). When under low torque conditions, PPAs considerably increased on a global scale, and the emergence of vortical flow structures within the vaneless space and inter-blade channels resulted into the appearance of two low frequency components namely 0.19*fn* and 1.19*fn* (*fn*: runner rotational frequency), for which the amplitudes are irregularly distributed along the runner inlet circumference, as shown in Figure 16 (b). When the runner inlet back flow vortices shifted to runner mid-span section under low flow conditions, vaneless space pressure fluctuation amplitudes shifted to lower values, where a new low frequency component emerged (0.39*fn*). This new component exhibited a comparatively periodically varying trend along the vaneless space circumference with higher amplitudes as compared to low torque conditions, which may implicate the existence of a rotating stall within these zones. Therefore, with a gradually decreasing flow, pressure pulsations within the vaneless space first increased from GVO21-OP4 to GVO21-OP6 and decrease to low flow conditions (GVO21-OP10). This decrease may have been caused by low flow-caused negligible momentum transfer between runner and guide vane flows, as compared to low torque situation. The distribution mode of different dominant frequency components within the vaneless space is shown in Figure 17. The BPF component exhibited the highest amplitudes, followed by 2BPF and then finally by 3BPF. As it is the case in the above sections, the amplitudes of each of the components increased to low torque conditions and then decreased towards low flow conditions. Due to a comparatively negligible level of incurred flow turbulences when operating under high flow conditions (OP4), the three dominant frequency components distribution under these conditions displayed a periodic variation tendency. This behavior was however found to be more

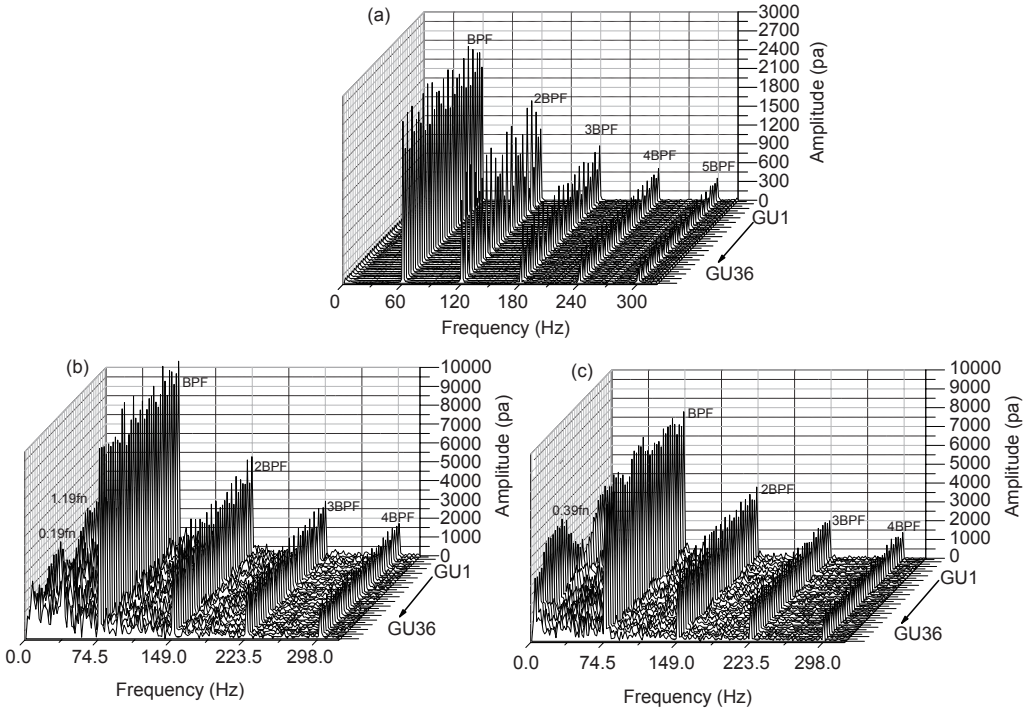

Figure 16 Vaneless space pressure pulsation frequency spectra for GVO21mm. (a) OP4; (b) OP6; (c) OP10.

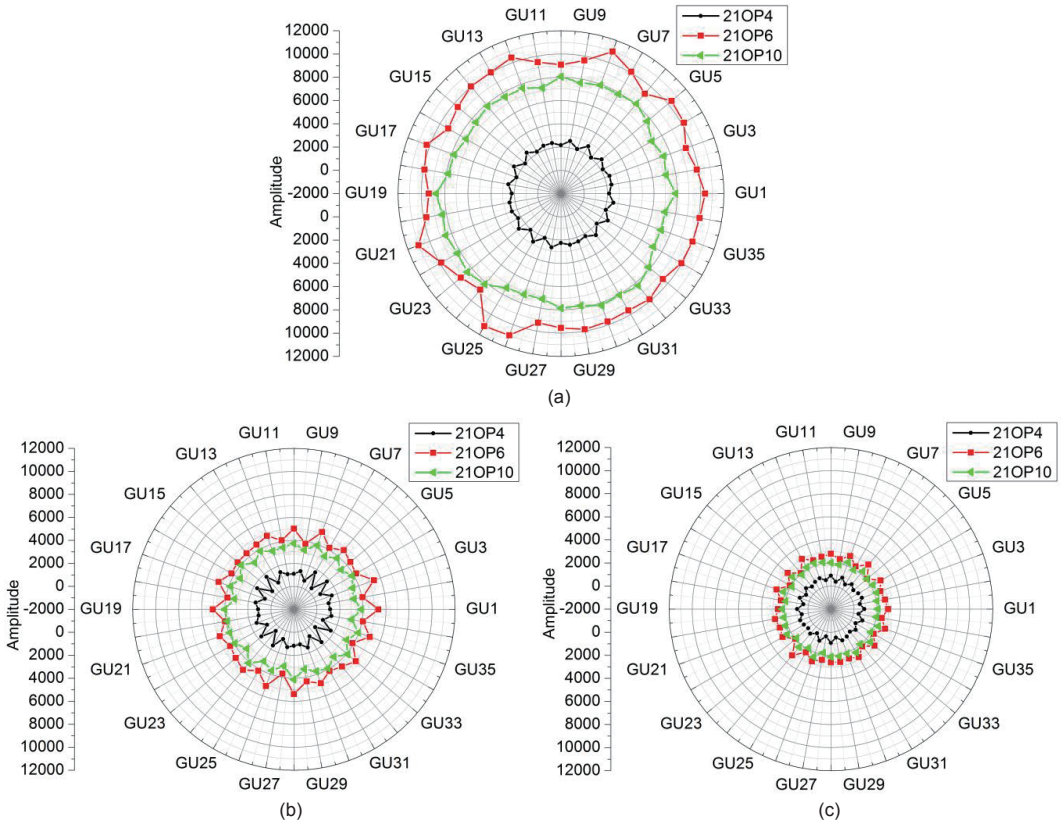

Figure 17 (Color online) Vaneless space pressure pulsation frequency components distribution. (a) 1BPF; (b) 2BPF; (c) 3BPF.

pronounced for the first and third dominant frequency respectively. The similarity between these two components' distribution (BPF and 3BPF) may also be having something to do with their respective contributions to RSI. Basing on the fact that the used RPT model disposes of 9 runner blades and 20 guide vanes, then it is obvious that both BPF and 3BPF components are contributed by the rotor (runner), while the 2BPF component takes origin from the stator (guide vanes). Figure 18 shows the RPPAs distribution along the flow channel for the three investigated GVOs. Following the flow path from the spiral casing inlet, PPAs keep a low profile with negligible point-to-point deviations all along the spiral casing (CP1A-CP4). Next, from the stay vanes zone inlet, PPAs start to gradually increase along the channel as the flow approaches the runner (ST6–ST2), before going through successive shifts to higher amplitude values in the guide vanes zone (GR4–GR1) where the peak is the runner inlet zones (GU9).

Note that the vaneless space PPAs are almost 2 to 5 times of those at the upstream flow zones. From the vaneless space through runner inter-blade channels downwards to flow zones at draft tube inlet vicinities (DR1), PPAs go through a free fall to very low values, followed by continuously decreasing PPAs from the draft tube inlet to the elbow. Therefore, for all operating conditions, pressure pulsations within the vaneless space between runner and guide vanes are the highest in the whole RPT flow passage. Moreover, just as it is the case for vaneless space pressure pulsations evolution, pulsation amplitudes increased from high flow conditions, reaching their peaks under low torque conditions and then decreased to low flow conditions. Pressure pulsation frequency spectra for monitors along the flow channels are shown in Figure 19. The blade passing frequency and its harmonics (2BPF and 3BPF) are still the dominant frequencies within the RPT flow channels. In addition, the earlier recorded low frequency components are still present within both the runner upstream and downstream flow zones for the three operating conditions. The dominant pressure pulsation frequencies within the draft tube are 0.19fn and its multiples (0.39fn, 0.57fn and so on) with 0.19fn being the draft tube first dominant frequency. Under high flow conditions, low frequency components can only be recorded within the draft tube. With an increased level of flow unsteadiness under low torque conditions, more low frequency components emerged within the runner upstream channels, where the two most remarkable components are multiples of the draft tube first dominant frequency (0.79fn≈4×0.19fn and 1.19fn≈6×0.19fn). Under low flow conditions, in line with the flow situation in Figures 8(b) and 9(b), pressure pulsation levels decreased and so were the concentration and number of low frequency components. Under these conditions, the only remarkable low frequency component is 0.39fn, which

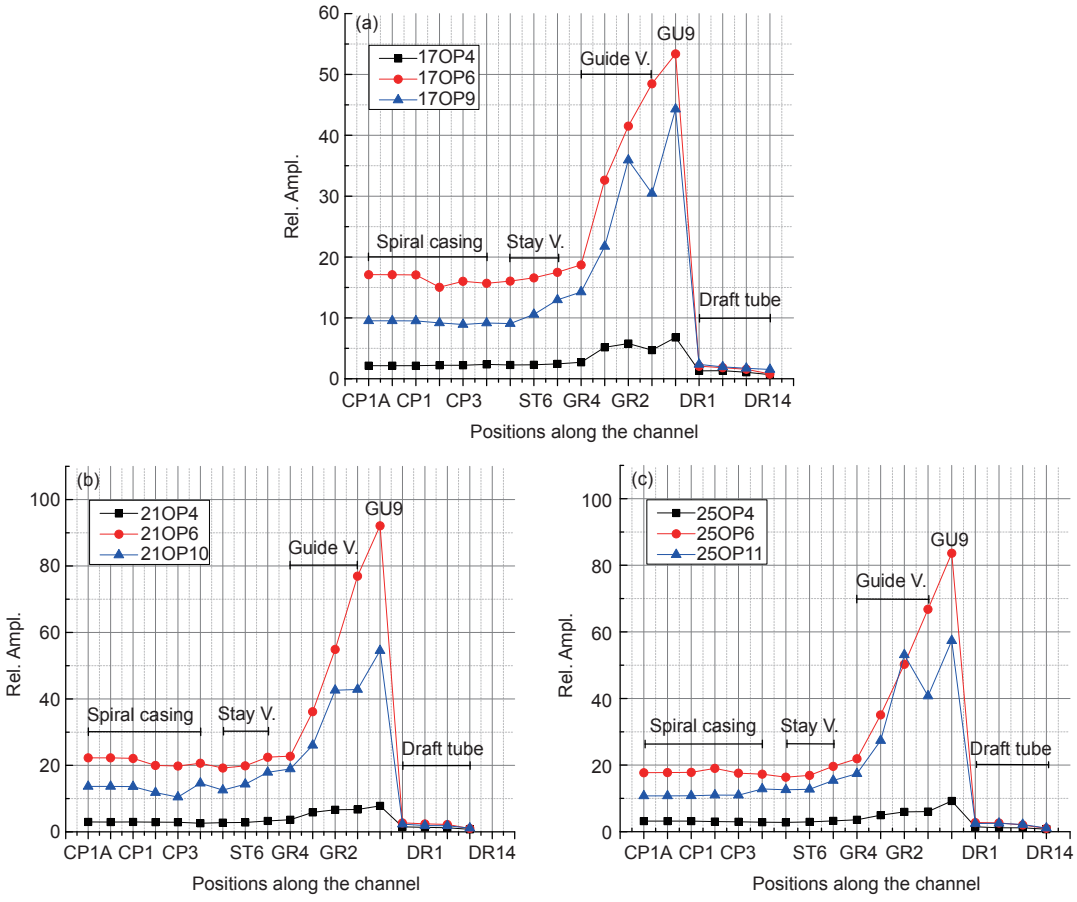

Figure 18 (Color online) Distribution of relative pressure fluctuation amplitudes along the flow channel for (a) GVO17mm, (b) GVO21mm, and (c) GVO25mm.

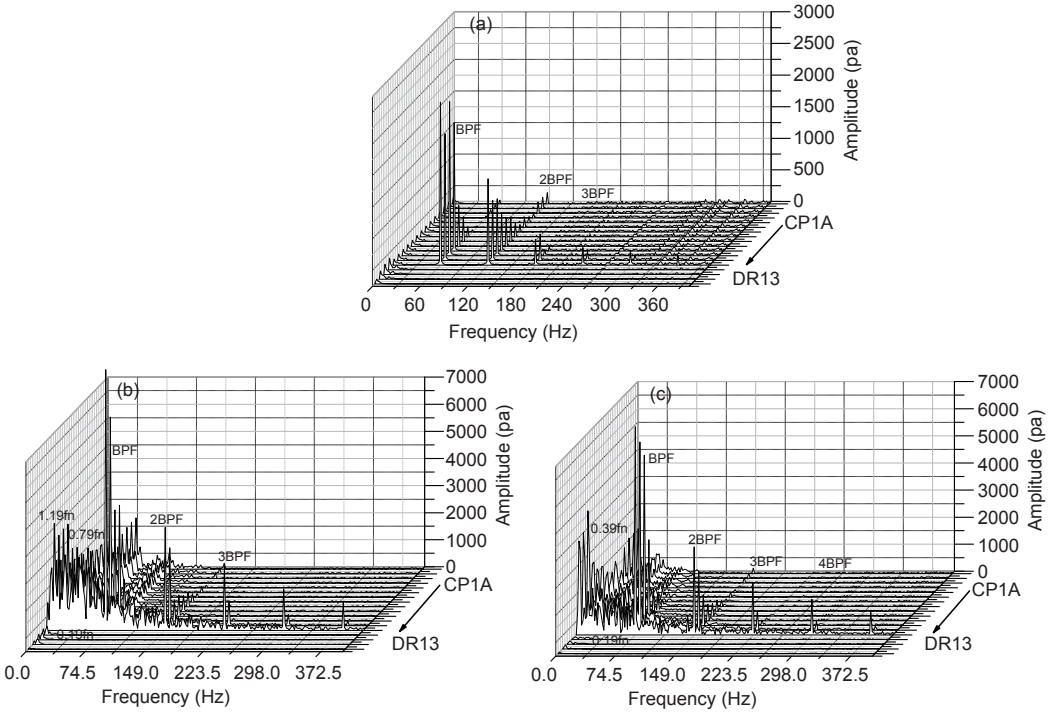

Figure 19 Pressure pulsation frequency spectra along the flow channel for (a) G21OP4 (b) G21OP6 and (c) G21OP10.

is also the double of the draft tube dominant frequency ($0.39fn \approx 2\times 0.19fn$). Note that all the recorded low frequency components have a close relationship with draft tube instabilities, and can be found within both the vaneless space and other RPT flow passages, with their amplitudes almost unchanged (undamped). This, however, is not the case when it comes to RSI-born BPF and its multiples, as shown in Figure 20. In this figure, the distribution of dominant frequencies (BPF, 2BPF and 3BPF) at different locations within the flow channels is presented. The BPF exhibits the highest fluctuation amplitudes, thus serving the first dominant frequency, where 2BPF and 3BPF are the second and third respectively.

For each of the dominant frequencies, amplitudes grow from high flow conditions, and get their peak values under low torque conditions, only to decrease again towards low flow conditions. Moreover, their amplitudes along the flow channel continuously dropped until they got to values close to zero at locations far enough from the vaneless space (spiral casing and draft tube). For instance, the amplitudes of BPF directly fall to zero in the draft tube and to values close to zero within the spiral casing, which is the case even for 2BPF [34]. On the other hand, 3BPF component is completely absent within the stay vanes and upstream locations as well as the draft tube flow channel. Therefore, in addition to low frequency components, the only pressure pulsation components available within flow channels at the upstream of the vaneless space for the three investigated conditions, are the damped BPF and 2BPF components.

In the next sections, an attempt has been done to comparatively analyze how the above discussed pressure pulsation behaviors can be impacted by the guide vane opening angle. Figure 21 shows the vaneless space RPPAs under three selected operating groups (GRO1, GRO2, and GRO4), for each of the guide vane openings. Under high flow conditions, pressure pulsations are symmetrically distributed with respect to the runner center of rotation. Moreover, vaneless space pressure pulsations are found to increase with the guide vane opening. The same situation persisted under low torque conditions; where however, pulsations distribution layout as well as corresponding amplitudes were completely same for both 21 and 25 mm openings, at the exception of monitoring points GU31 and GU32 at the flow zones next to the special vane location (Figure 21(b)). However, this guide vane opening-based pressure pulsation distribution law did not hold for low flow conditions, where the RPT model with 21 mm GVO exhibited the highest PPAs at most of vaneless space monitoring points, followed by 25 and 17 mm GVOs respectively(Figure 18(c)). In the same context, low flow conditions for every guide vane opening

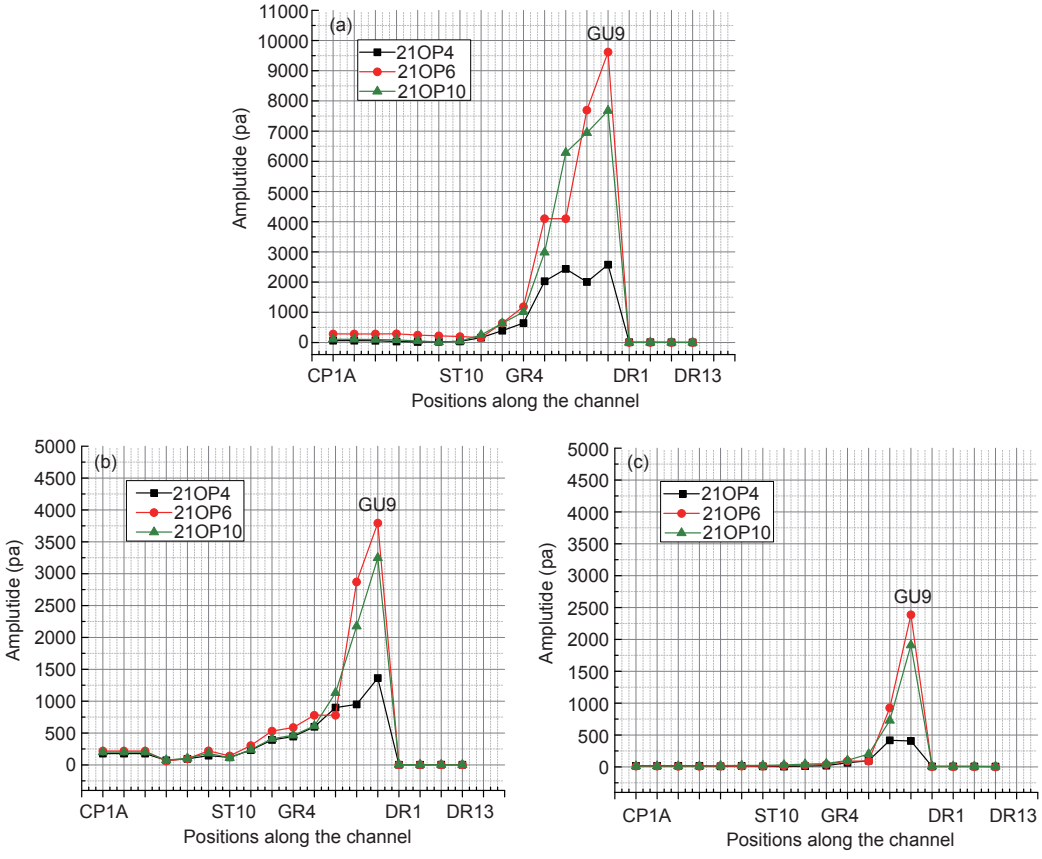

Figure 20 Pressure pulsation frequency components distribution along the flow channel. (a) 1BPF; (b) 2BPF; (c) 3BPF.

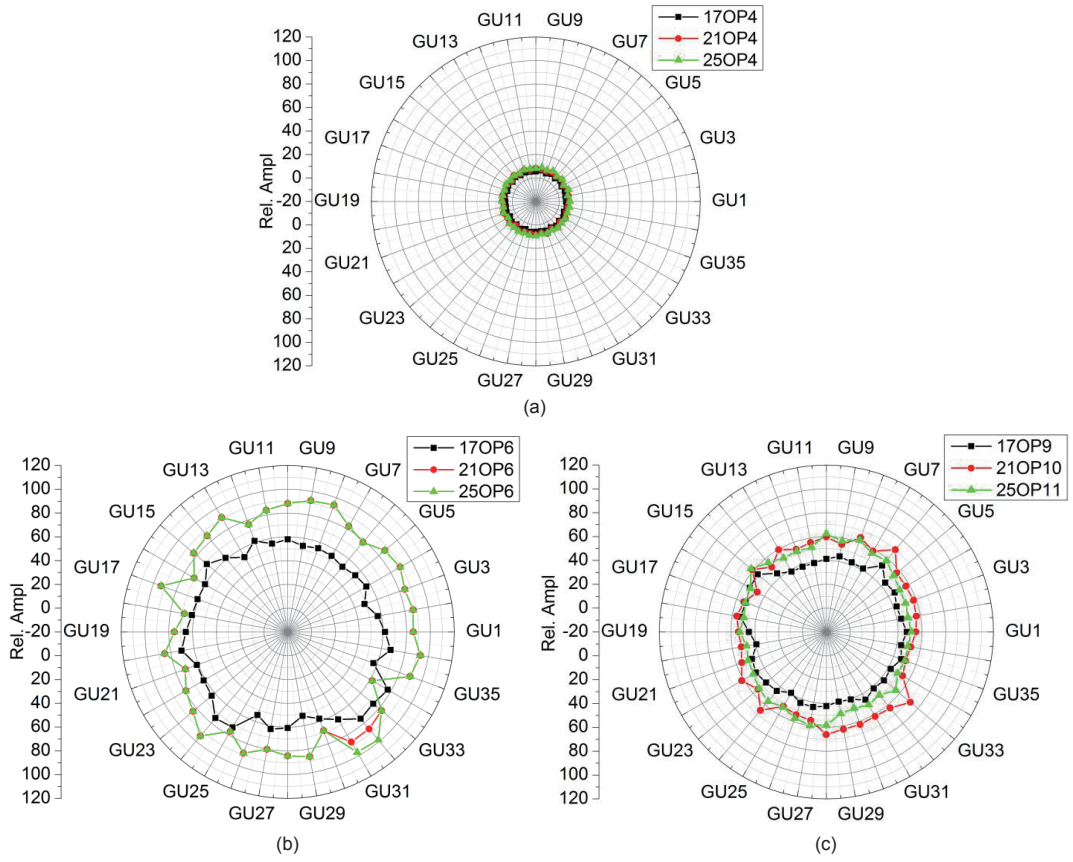

Figure 21 (Color online) Vaneless space relative pressure pulsation amplitudes distribution for (a) GRO1, (b) GRO2, and (c) GRO4.

have been selected for farther analysis. Pressure pulsation spectra within vaneless space zones under low flow conditions for each of the three investigated guide vane openings, are shown in Figure 22. Owing to the fact the three presented cases are all low flow conditions; low frequency pressure pulsation frequency components are present for each case. Moreover, a big number of high frequency-low amplitude components (between BPF and 3BPF) can also be noticed. While low frequency components under 17 mm GVO are of almost the same amplitude where none of them exhibited a remarkably higher amplitude than the others; when the GVO increased to 21 mm, a new low frequency component (0.39*fn*) emerged and a corresponding global increase of PPAs was obvious. Under the 25 mm GVO, the above stated 0.39*fn* low frequency component remained, where a newly risen one (0.59*fn*) added up making it two low frequency components with higher amplitudes than the precedent case, under these conditions. In addition to the increase with of the number of low frequency components, the GVO increased also heightened the global PPAs on the whole range of available pressure pulsation frequencies. Figure 23 shows the distribution of dominant pressure pulsation frequency components (BPF, 2BPF, and 3BPF) within the vaneless space flow zones. Pulsation amplitudes of the BPF component were found to increase with GVO, where the amplitudes under 17 mm GVO are lower than the remaining two GVOs at most of vaneless space monitoring points. Moreover, BPF amplitudes under 21 mm GVO and 25 mm GVO have been very close or even equal at different locations in the vaneless gap, but also at many more locations the 25 mm GVO exhibited higher amplitudes than the 21 mm GVO. On the other side, the vaneless space pulsation amplitudes distribution of 2BPF components for the three openings, presented periodic characteristics where at the exception of a few locations, the similarity in amplitude variation trend is quite noticeable.

Moreover, despite the complexity in the variation of amplitudes distribution for the three openings, it is could be seen that at many locations the highest amplitudes were achieved by the 25 mm GVO while the lowest happened with the 17 mm GVO, a fact which still confirms the PPA changing law as shown on the BPF variation case. For the 3BPF component, as shown in Figure 23(c), the pulsation amplitudes distribution is a bit more concentric, where pulsations with the 17 mm GVO are obviously the lowest, while pulsation amplitudes distribution for the two remaining openings are quite self-crossing and fluctuate almost within the same pressure amplitude range at different locations. The noticed global increase in vaneless space pressure pulsation with the GVO increase is connected to the corresponding flow unsteadiness increase at the same zones. With the GVO

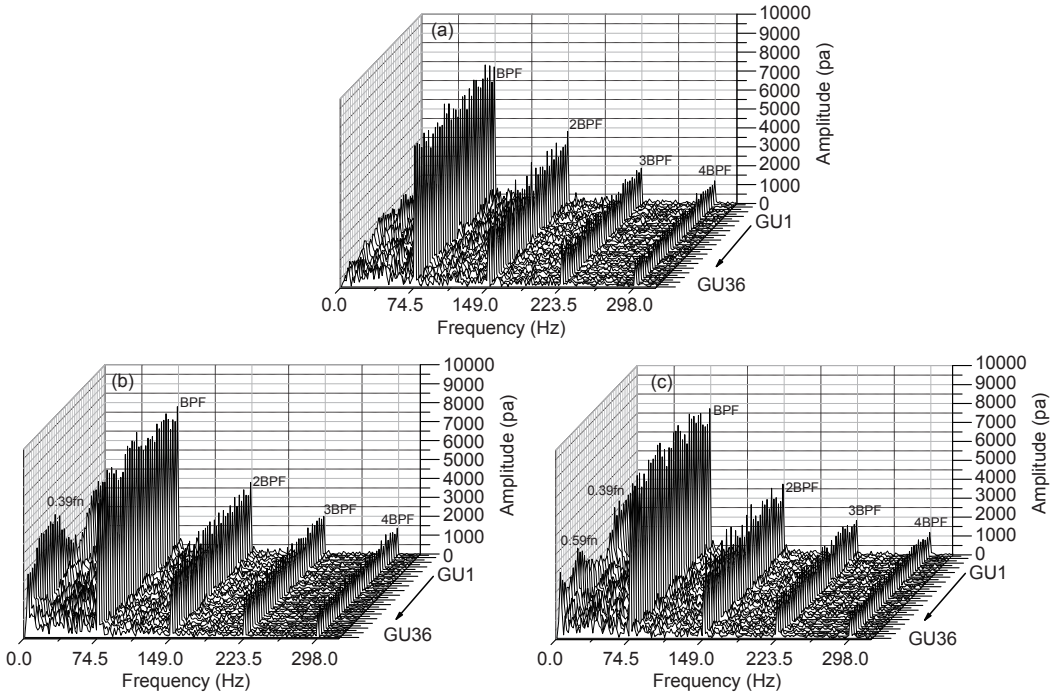

Figure 22 Vaneless space pressure pulsation frequency spectra for (a) GVO17-OP9, (b) GVO21-OP10, and (c) GVO25-OP11.

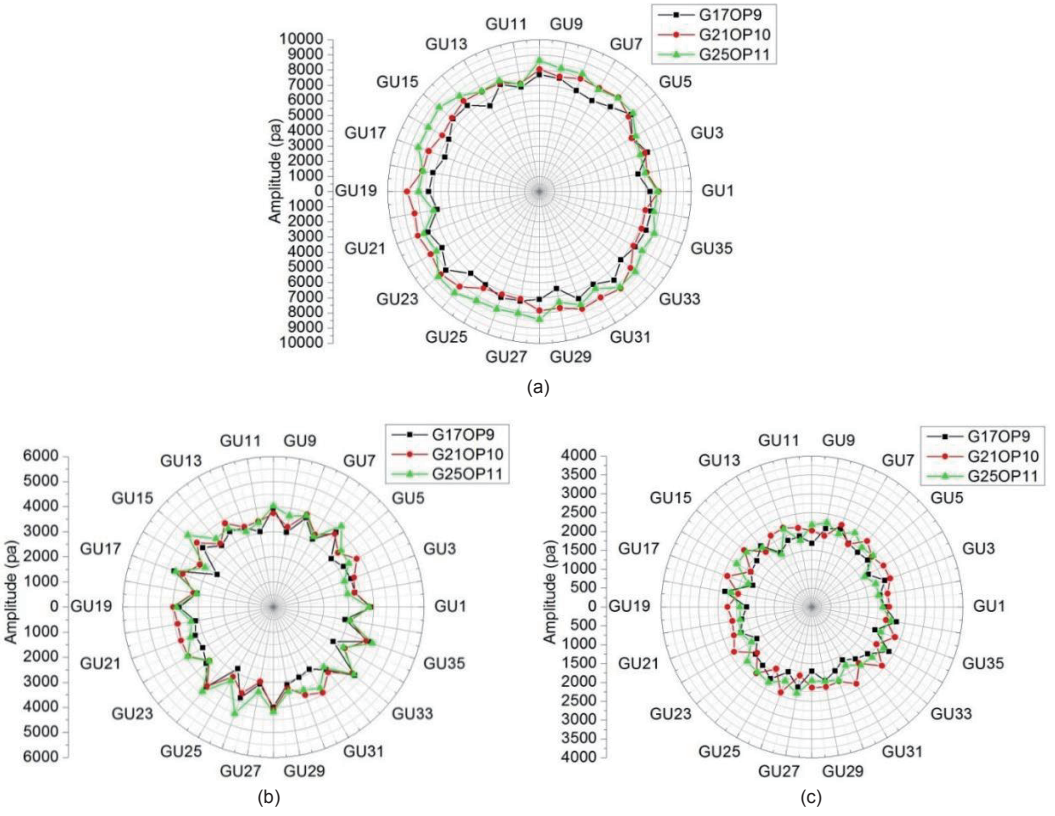

Figure 23 (Color online) Vaneless space pressure pulsation frequency components distribution for GRO4. (a) BPF; (b) 2BPF; (c) 3BPF.

increase, the inter-vane channel size gradually widens up, leading to inter-vane channel flow velocity decrease as well as the change of flow incidence angle at the runner inlet, all leading to different vaneless space flow separations occurrence. In addition, the corresponding vaneless space thinning leads to the intensification of rotor-stator interactions, which

in turn induces even more pressure pulsations at the same zones. In Figure 24, the variation trend of RPPAs along the flow channel under low flow conditions for the three investigated GVOs is shown. It can be seen that the RPT model with 21 mm model experienced the highest pressure pulsation levels within the stay vanes and upstream flow zones. However, for the remaining locations along the flow path (vaneless space and draft tube), pressure pulsation with 25 mm GVO were the highest, followed 21 mm GVO and finally by 17 mm GVO. Note that vaneless space pressure pulsation levels are far higher than any other location along the flow path (80% to 84%). In other words, one would conclude that pressure pulsation levels along the flow channel increased with the GVO. Figure 25 presents the pressure pulsation frequency spectra at different locations within the flow channel from the spiral casing all along downstream to the draft tube for the three studied GVOs. In the same context as the above discussed vaneless space GVO-based pressure pulsation level variations, PPAs within the flow channel for both dominant and low frequency components, increased with the GVO. Moreover, the same previously discussed vaneless space low frequency components (0.39*fn* for 21 mm GVO, and 0.39*fn* and 0.59*fn* for 25 mm GVO) are also present within the flow zones along the flow path.

The distribution of dominant frequency components along the flow channel for the three openings is shown in Figure 26. The BPF component distribution trend is quite similar for all the openings at the exception of GR1 monitoring point

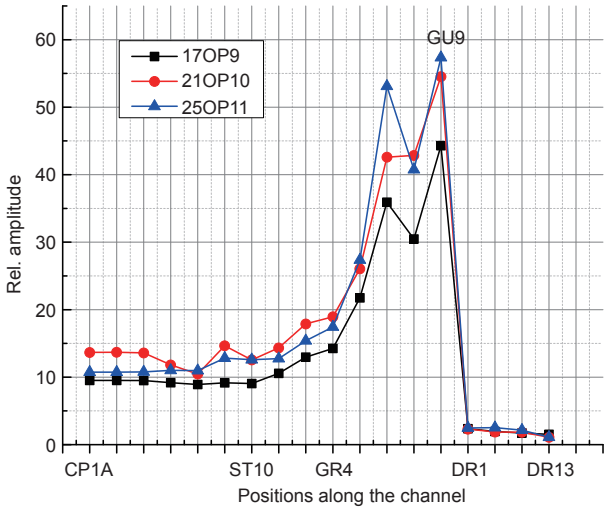

Figure 24 (Color online) Relative pressure pulsation amplitude distribution along the flow channel within GRO4 operating group.

within the vaneless space. The peak of BPF amplitudes along the flow channel is at the vaneless space, while the amplitudes at the vaneless space's far upstream and downstream locations are negligible (close to zero) and null respectively. The BPF being the first dominant frequency for all openings, its amplitude distribution is quite similar to the global distribution of pressure pulsation levels along the flow channel as shown in Figure 24. This similarity is more pronounced at monitoring points within both the vaneless space and inter-guide vane flow zones. The BPF amplitudes are therefore

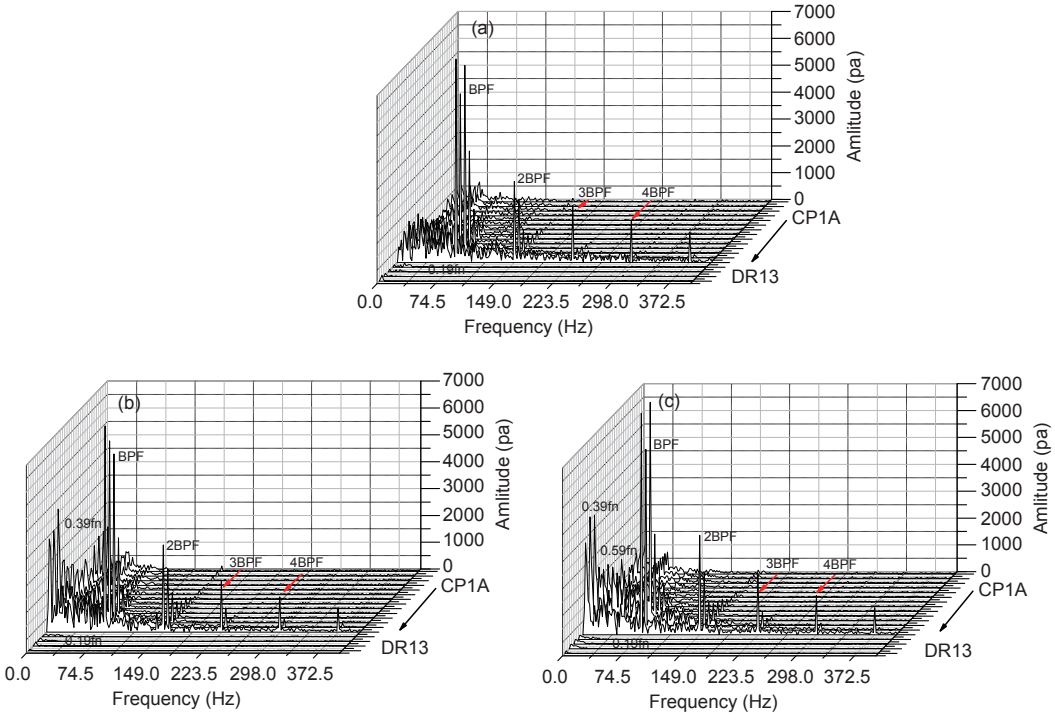

Figure 25 Pressure pulsation frequency spectra along the flow channel for (a) GVO17mm-OP9, (b) GVO21mm-OP10, and (c) GVO25mm-OP11.

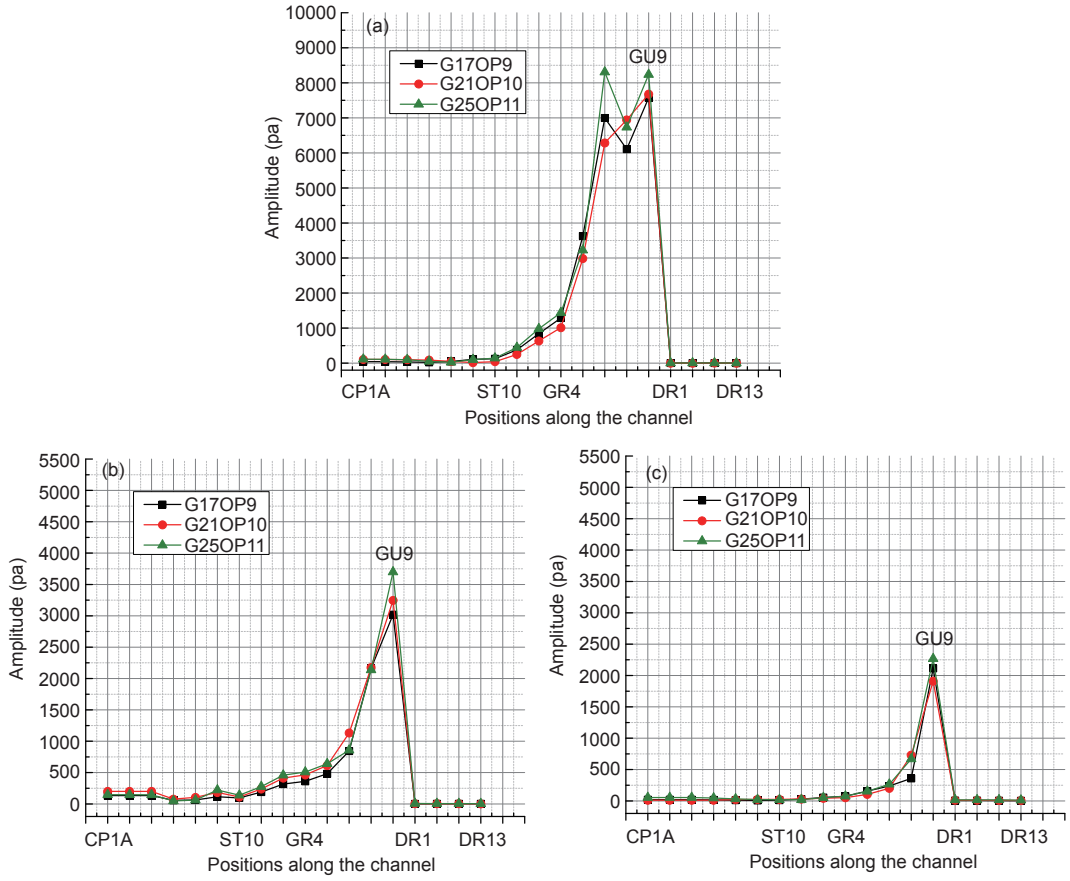

Figure 26 (Color online) Pressure pulsation frequency components distribution along the flow channel. (a) 1BPF; (b) 2BPF; (c) 3BPF.

found to generally increase with the GVO. The same principle holds even for 2BPF (second dominant frequency), where however, the amplitudes within far upstream flow zones were a bit higher than the BPF case, and 21 mm GVO associated amplitudes were the highest within the spiral casing. As for the 3BPF component, being the 3rd dominant frequency, its amplitudes were found to very quickly drop as compared to other components, where for instance its amplitudes fall to very low values at flow zones within the guide vanes, which continues to be the case even in the upstream zones. For this component again, the highest amplitude values were still associated with the 25 mm GVO, whereas the lowest value was associated to the 21 mm GVO. Note that for the three investigated GVO, the amplitudes of all available pressure pulsation dominant frequencies within the draft tube were null.

4 Conclusions

The presented study is a 3D numerical simulation of the RPT turbulent flow under three different guide vane openings namely 17, 21, and 25 mm. It was carried out to investigate the onset and development mechanism of flow instability and associated pressure pulsation characteristics within a RPT complete flow passage. Four operating conditions were investigated, expanding from turbine zone (GRO1) through low torque (GRO2 and GRO3) to turbine brake zone (GRO4). The following conclusions are drawn.

(1) With the gradually changing machine operating conditions from turbine to turbine brake zone, blade suction side-attached vortex flow first emerges within runner inter-blade channels. With a continuously decreasing flow, the later first weakens and shifts to blade pressure side, while back flow vortices emerge at the runner inlet zone's hub side. At runaway vicinities and turbine brake zones, the inter-blade channel vortex flow gets serious, completely blocking some runner channels, while the runner inlet back flow vortices shift their positions from hub to the mid-span zones, marking the presence of a rotating stall. The above mentioned shift of vortex flow location from blade suction side to pressure side takes source from the change of flow incidence angle at the runner inlet, as the flow decreased. On the other hand, the emergence of runner inlet back flow vortices is believed to originate from a continuous flow velocity's radial component decrease, as the runner rotational speed increased. The RPT flow dynamics are found to be considerably sensitive to guide vane opening changes, where

with a gradual guide vane opening increase, the runner inter-blade channel flow vortices tend to weaken while the vaneless space flow unsteadiness correspondingly worsens.

(2) With a continuously decreasing flow, RPT pressure pulsations first increase to their peak values under low torque operating conditions and then decrease to low flow conditions. Along the RPT full flow passage from the spiral casing inlet to the draft tube outlet, the highest pressure pulsations are based in the vaneless space between the runner and guide vanes. These ones take source from both the RSI and the operating conditions-dependent flow unsteadiness within the same zones. However, at the exception of vaneless space flow instability-linked low frequency components, the RSI-born pressure pulsation dominant frequency components, which are the BPF and its harmonics (2BPF and 3BPF), are directly damped to very low amplitude values at upstream flow zones. In addition, low frequency pressure pulsation components in the runner upstream zones are closely related to draft tube flow unsteadiness as they generally are multiples of draft tube dominant pressure pulsation frequency (0.19*fn*). Pressure pulsations within RPT flow zones are globally found to increase with the guide vane opening.

This work was supported by the National Natural Science Foundation of China (Grant No. 51606050), Chinese Postdoctoral Science Foundation (Grant No. 2016M591527), Heilongjiang Postdoctoral Fund (Grant No. LBH-Z16057), Natural Science Foundation of Heilongjiang Province (Grant No. E2017038), and the Fundamental Research Funds for the Central Universities (Grant No. HIT.NSRIF.2019062).

1 Sammartano V, Aricò C, Carravetta A, et al. Banki-michell optimal design by computational fluid dynamics testing and hydrodynamic analysis. Energies, 2013, 6: 2362–2385
2 Chen T, Zhang Y, Li S. Instability of large-scale prototype francis turbines of three gorges power station at part load. Proc Inst Mech Eng Part A-J Power Energy, 2016, 230: 619–632
3 Hamududu B, Killingtveit A. Assessing climate change impacts on global hydropower. Energies, 2012, 5: 305–322
4 Binama M, Su W T, Li X B, et al. Investigation on pump as turbine (PAT) technical aspects for micro hydropower schemes: A state-of-the-art review. Renew Sustain Energy Rev, 2017, 79: 148–179
5 Munoz-Hernandez G A, Mansoor S P, Jones D I. Modelling and Controlling Hydropower Plants. 1 ed. London: Springer-Verlag, 2013
6 Zhang Y, Zhang Y, Wu Y. A review of rotating stall in reversible pump turbine. Proc Inst Mech Eng Part C-J Mech Eng Sci, 2017, 231: 1181–1204
7 Beaudin M, Zareipour H, Schellenberglabe A, et al. Energy storage for mitigating the variability of renewable electricity sources: An updated review. Energy Sustain Dev, 2010, 14: 302–314
8 Yao E, Wang H, Liu L, et al. A novel constant-pressure pumped hydro combined with compressed air energy storage system. Energies, 2015, 8: 154–171
9 Sundararagavan S, Baker E. Evaluating energy storage technologies for wind power integration. Sol Energy, 2012, 86: 2707–2717
10 Sarasúa J, Pérez-Díaz J, Torres Vara B. On the implementation of variable speed in pump-turbine units providing primary and secondary load-frequency control in generating mode. Energies, 2015, 8: 13559–13575
11 Zhang Y, Liu K, Li J, et al. Analysis of the vortices in the inner flow of reversible pump turbine with the new omega vortex identification method. J Hydrodyn, 2018, 30: 463–469
12 Díaz-González F, Sumper A, Gomis-Bellmunt O, et al. A review of energy storage technologies for wind power applications. Renew Sustain Energy Rev, 2012, 16: 2154–2171
13 Valero C, Egusquiza M, Egusquiza E, et al. Extension of operating range in pump-turbines. Influence of head and load. Energies, 2017, 10: 2178
14 Yin J, Wang D, Kim Y T, et al. A hybrid energy storage system using pump compressed air and micro-hydro turbine. Renew Energy, 2014, 65: 117–122
15 Zhang Y, Zheng X, Li J, et al. Experimental study on the vibrational performance and its physical origins of a prototype reversible pump turbine in the pumped hydro energy storage power station. Renew Energy, 2019, 130: 667–676
16 Zhang Y, Zhang Y, Qian Z, et al. A review of microscopic interactions between cavitation bubbles and particles in silt-laden flow. Renew Sustain Energy Rev, 2016, 56: 303–318
17 Lai X D, Liang Q W, Ye D X, et al. Experimental investigation of flows inside draft tube of a high-head pump-turbine. Renew Energy, 2019, 133: 731–742
18 Soder L, Abildgaard H, Estanqueiro A, et al. Experience and challenges with short-term balancing in european systems with large share of wind power. IEEE Trans Sustain Energy, 2012, 3: 853–861
19 Zhang Y, Chen T, Li J, et al. Experimental study of load variations on pressure fluctuations in a prototype reversible pump turbine in generating mode. J Fluids Eng, 2017, 139: 074501
20 Jacquet C, Fortes-Patella R, Balarac L, et al. CFD investigation of complex phenomena in S-shape region of reversible pump-turbine. IOP Conf Ser-Earth Environ Sci, 2016, 49: 042010
21 Tanaka H. Vibration behaviour and dynamic stress of runners of very high head reversible pump-turbines. In: Proceedings of the 15th IAHR Symp. Belgrade-Yugoslavia, 1990
22 Egusquiza E, Valero C, Huang X, et al. Failure investigation of a large pump-turbine runner. Eng Failure Anal, 2012, 23: 27–34
23 Gentner C, Sallaberger M, Widmer C, et al. Numerical and experimental analysis of instability phenomena in pump turbines. IOP Conf Ser-Earth Environ Sci, 2012, 15: 032042
24 Yin J L, Wang D Z, Walters D K, et al. Investigation of the unstable flow phenomenon in a pump turbine. Sci China Phys Mech Astron, 2014, 57: 1119–1127
25 Guggenberger M F S, Jürgen S, Helmut J, et al. Investigating the dynamic aspects of the turbine instability of a pump turbine model. In: Proceedings of the 6th IAHR International Meeting of the Workgroup on Cavitation and Dynamic Problems in Hydraulic Machinery and Systems. Ljubljana-Slovenia, 2015. 9–11
26 Hasmatuchi V, Farhat M, Maruzewski P, et al. Experimental investigation of a pump-turbine at off-design operating conditions. In: Proceedings of the 3rd International Meeting of the Workgroup on Cavitation and Dynamic Problems in Hydraulic Machinery and Systems. Brno: Brno University of Technology, 2009
27 Hasmatuchi V, Farhat M, Roth S, et al. Experimental evidence of rotating stall in a pump-turbine at off-design conditions in generating mode. J Fluids Eng, 2011, 133: 051104
28 Wang L Q, Yin J L, Jiao L, et al. Numerical investigation on the "S" characteristics of a reduced pump turbine model. Sci China Tech Sci, 2011, 54: 1259–1266
29 Botero F, Guzman S, Hasmatuchi V, et al. Flow visualization approach for periodically reversed flows. J Flow Vis Image Proc, 2012, 19: 309–321
30 Li Z, Bi H, Wang Z, et al. Three-dimensional simulation of unsteady flows in a pump-turbine during start-up transient up to speed no-load condition in generating mode. Proc Inst Mech Eng Part A-J Power Energy, 2016, 230: 570–585
31 Wang Z, Zhu B, Wang X, et al. Pressure fluctuations in the S-shaped region of a reversible pump-turbine. Energies, 2017, 10: 96
32 Cavazzini G, Covi A, Pavesi G, et al. Analysis of the unstable be-

havior of a pump-turbine in turbine mode: fluid-dynamical and spectral characterization of the S-shape characteristic. J Fluids Eng, 2015, 138: 021105
33 Widmer C, Staubli T, Ledergerber N. Unstable characteristics and rotating stall in turbine brake operation of pump-turbines. J Fluids Eng, 2011, 133: 041101
34 Zobeiri A, Kueny J L, Farhat M, et al. Pump-turbine rotor-stator interactions in generating mode: Pressure fluctuation in distributor channel. In: Proceedings of the 23rd IAHR Symposium on Hydraulic Machinery and Systems. Yokohama, 2006. 1–10
35 Liu J S, Guan R Q. Experimental study of pressure fluctuations in francis pump-turbines. Tsinghua Sci Rep (TH83021). Beijing, 1983
36 Sun H, Xiao R, Wang F, et al. Analysis of the pump-turbine S characteristics using the detached eddy simulation method. Chin J Mech Eng, 2015, 28: 115–122
37 Rezghi A, Riasi A. The interaction effect of hydraulic transient conditions of two parallel pump-turbine units in a pumped-storage power plant with considering "S-shaped" instability region: Numerical simulation. Renew Energy, 2018, 118: 896–908
38 Hu J, Yang J, Zeng W, et al. Transient pressure analysis of a prototype pump turbine: Field tests and simulation. J Fluids Eng, 2018, 140: 071102
39 Liu Y, Tan L, Liu M, et al. Influence of Prewhirl Angle and Axial Distance on Energy Performance and Pressure Fluctuation for a Centrifugal Pump with Inlet Guide Vanes. Energies, 2017, 10: 695, doi: 10.3390/en10050695
40 Liu Y, Tan L, Hao Y, et al. Energy performance and flow patterns of a mixed-flow pump with different tip clearance sizes. Energies, 2017, 10: 191
41 Olimstad G, Nielsen T, Børresen B. Dependency on runner geometry for reversible-pump turbine characteristics in turbine mode of operation. J Fluids Eng, 2012, 134: 121102
42 Yin J, Wang D, Wei X, et al. Hydraulic improvement to eliminate S-shaped curve in pump turbine. J Fluids Eng, 2013, 135: 071105
43 Zhu B, Tan L, Wang X, et al. Investigation on flow characteristics of pump-turbine runners with large blade lean. J Fluids Eng, 2017, 140: 031101
44 Liu L, Zhu B, Bai L, et al. Parametric design of an ultrahigh-head pump-turbine runner based on multiobjective optimization. Energies, 2017, 10: 1169
45 Pavesi G, Cavazzini G, Ardizzon G. Time-frequency characterization of rotating instabilities in a centrifugal pump with a vaned diffuser. Int J Rot Machin, 2008, 2008(3): 1–10
46 Mao X, Dal Monte A, Benini E, et al. Numerical study on the internal flow field of a reversible turbine during continuous guide vane closing. Energies, 2017, 10: 988
47 Li D, Wang H, Li Z, et al. Transient characteristics during the closure of guide vanes in a pump-turbine in pump mode. Renew Energy, 2018, 118: 973–983
48 Fu X, Li D, Wang H, et al. Analysis of transient flow in a pump-turbine during the load rejection process. J Mech Sci Technol, 2018, 32: 2069–2078
49 Fu X, Li D, Wang H, et al. Influence of the clearance flow on the load rejection process in a pump-turbine. Renew Energy, 2018, 127: 310–321
50 Cavazzini G, Houdeline J B, Pavesi G, et al. Unstable behaviour of pump-turbines and its effects on power regulation capacity of pumped-hydro energy storage plants. Renew Sustain Energy Rev, 2018, 94: 399–409
51 Li J, Zhang Y, Liu K, et al. Numerical simulation of hydraulic force on the impeller of reversible pump turbines in generating mode. J Hydrodyn, 2017, 29: 603–609
52 Gong R, Li D, Wang H, et al. Investigation into the flow details of runner region in a pump turbine at off-design conditions. Adv Mech Eng, 2016, 8: 168781401663072
53 Zhu D, Xiao R, Tao R, et al. Impact of guide vane opening angle on the flow stability in a pump-turbine in pump mode. Proc Inst Mech Eng Part C-J Mech Eng Sci, 2017, 231: 2484–2492
54 International Electrotechnical Commission. Hydraulic turbines, storage pumps and pump-turbines—model acceptance tests. Standard No. IEC, 60193. Geneva, 1999
55 Jones W P, Launder B E. The prediction of laminarization with a two-equation model of turbulence. Int J Heat Mass Transfer, 1972, 15: 301–314
56 Wilcox D C. Reassessment of the scale-determining equation for advanced turbulence models. AIAA J, 1988, 26: 1299–1310
57 Woelke M. Eddy viscosity turbulence models employed by computational fluid dynamics. Trans Inst Aviat, 2007
58 Menter F R. Two-equation eddy-viscosity turbulence models for engineering applications. AIAA J, 1994, 32: 1598–1605
59 Menter F, Rumsey C. Assessment of two-equation turbulence models for transonic flows. In: Proceedings of Fluid Dynamics Conference. American Institute of Aeronautics and Astronautics, 1994. 2343
60 Blazek J. Chapter 7: Turbulence modelling. In: Blazek J, ed. Computational Fluid Dynamics: Principles and Applications. 2nd ed. Oxford: Elsevier Science, 2005. 227–270
61 Yang D D, Luo X W, Liu D M, et al. Unstable flow characteristics in a pump-turbine simulated by a modified Partially-Averaged Navier-Stokes method. Sci China Tech Sci, 2019, 62: 406–416
62 Yin J L, Liu J T, Wang L Q, et al. Performance prediction and flow analysis in the vaned distributor of a pump turbine under low flow rate in pump mode. Sci China Tech Sci, 2010, 53: 3302–3309
63 Li D, Wang H, Qin Y, et al. Mechanism of high amplitude low frequency fluctuations in a pump-turbine in pump mode. Renew Energy, 2018, 126: 668–680
64 Li D, Wang H, Qin Y, et al. Numerical simulation of hysteresis characteristic in the hump region of a pump-turbine model. Renew Energy, 2018, 115: 433–447
65 Dong X, Wang Y, Chen X, et al. Determination of epsilon for Omega vortex identification method. J Hydrodyn, 2018, 30: 541–548
66 Zhang Y, Liu K, Xian H, et al. A review of methods for vortex identification in hydroturbines. Renew Sustain Energy Rev, 2018, 81: 1269–1285
67 Guo L, Liu J T, Wang L Q, et al. Pressure fluctuation propagation of a pump turbine at pump mode under low head condition. Sci China Tech Sci, 2014, 57: 811–818
68 Li J W, Zhang Y N, Yu J X. Experimental investigations of a prototype reversible pump turbine in generating mode with water head variations. Sci China Tech Sci, 2018, 61: 604–611
69 Fu X L, Li D Y, Wang H J, et al. Dynamic instability of a pump-turbine in load rejection transient process. Sci China Tech Sci, 2018, 61: 1765–1775